

*The development of a space climatology:
3. Models of the evolution of distributions
of space weather variables with timescale*

Article

Accepted Version

Lockwood, M. ORCID: <https://orcid.org/0000-0002-7397-2172>,
Bentley, S. N., Owens, M. J. ORCID: <https://orcid.org/0000-0003-2061-2453>, Barnard, L. A. ORCID:
<https://orcid.org/0000-0001-9876-4612>, Scott, C. J. ORCID:
<https://orcid.org/0000-0001-6411-5649>, Watt, C. E., Allanson,
O. and Freeman, M. P. (2019) The development of a space
climatology: 3. Models of the evolution of distributions of space
weather variables with timescale. *Space Weather*, 17 (1). pp.
180-209. ISSN 1542-7390 doi:
<https://doi.org/10.1029/2018SW002017> Available at
<https://centaur.reading.ac.uk/81043/>

It is advisable to refer to the publisher's version if you intend to cite from the work. See [Guidance on citing](#).

To link to this article DOI: <http://dx.doi.org/10.1029/2018SW002017>

Publisher: American Geophysical Union

All outputs in CentAUR are protected by Intellectual Property Rights law, including copyright law. Copyright and IPR is retained by the creators or other copyright holders. Terms and conditions for use of this material are defined in

the [End User Agreement](#).

www.reading.ac.uk/centaur

CentAUR

Central Archive at the University of Reading

Reading's research outputs online

The development of a space climatology: 3. Models of the evolution of distributions of space weather variables with timescale

Mike Lockwood¹, Sarah N. Bentley¹, Mathew J. Owens¹, Luke A. Barnard¹,
Chris J. Scott¹, Clare E. Watt¹, Oliver Allanson¹ and Mervyn P. Freeman²

¹Department of Meteorology, University of Reading, Earley Gate, P.O. Box 243, Reading, Berkshire, RG6 6BB, UK.

²British Antarctic Survey, High Cross, Madingley Road, Cambridge, CB3 0ET, UK.

Corresponding author: M. Lockwood (m.lockwood@reading.ac.uk)

Key Points:

- Core distributions and extreme events of geomagnetic activity are studied as a function of averaging timescale τ
- The autocorrelation is shown to have a dominant role determining how these core distributions vary with averaging timescale τ
- Models for computing the distribution of geomagnetic activity for a given timescale τ and annual mean are presented

Abstract

We study how the probability distribution functions of power input to the magnetosphere P_α and of the geomagnetic ap and Dst indices vary with averaging timescale, τ , between 3 hours and 1 year. From this we develop and present algorithms to empirically model the distributions for a given τ and a given annual mean value. We show that lognormal distributions work well for ap , but because of the spread of Dst for low activity conditions, the optimum formulation for Dst leads to distributions better described by something like the Weibull formulation. Annual means can be estimated using telescope observations of sunspots and modelling, and so this allows the

25 distributions to be estimated at any given τ between 3 hour and 1 year for any of the past 400 years,
 26 which is another important step towards a useful space weather climatology. The algorithms apply
 27 to the core of the distributions and can be used to predict the occurrence rate of “large” events (in
 28 the top 5% of activity levels): they may contain some, albeit limited, information relevant to
 29 characterizing the much rarer “superstorm” events with extreme value statistics. The algorithm for
 30 the *Dst* index is the more complex one because, unlike *ap*, *Dst* can take on either sign and future
 31 improvements to it are suggested.

32 **1. Introduction**

33 This paper is the third of a series of three that is aimed at putting in place some of the key elements
 34 that will be needed to build a space weather climatology that covers both grand solar maximum and
 35 grand solar minimum conditions. As discussed in the introductions to Papers 1 and 2 [*Lockwood et*
 36 *al.*, 2018b; c], information on space climate over an interval long enough to cover both a grand
 37 solar minimum and a grand solar maximum (of order 400 years) is available only in the form of
 38 modelled annual means of some key variables [*Owens et al.*, 2017]. Hence developing a
 39 climatology giving the probability of space weather events of a given geoeffectiveness that covers
 40 both these extremes of the long-term solar variation requires us to develop an understanding of
 41 relationships between these annual means and the distributions of event amplitudes, quantified over
 42 the relevant timescales. Because space weather events come in bursts, the integrated value of any
 43 activity index X over the most relevant timescale τ , I_X , is a useful metric [*Echer et al.*, 2008;
 44 *Lockwood et al.*, 2016; *Borovsky*, 2017; *Tindale et al.*, 2018], and this equals the arithmetic mean
 45 value times τ (i.e., $I_X = \int_{\tau} X dt = \tau \langle X \rangle_{\tau}$). Hence it is important to study how $\langle X \rangle_{\tau}$ varies with τ and
 46 how it relates to the annual arithmetic mean value $\langle X \rangle_{\tau=1\text{yr}}$. *Lockwood et al.* [2018a] have
 47 demonstrated how annual means can be used to quantify the frequency of geomagnetic disturbance
 48 events above a given (large but not extreme) threshold for the past 400 years, but they studied only
 49 hourly and daily means ($\tau = 1$ hr and $\tau = 1$ day) which, in general, will not be the most relevant
 50 timescales for all space weather phenomenon. For example, *Lockwood et al.* [2016] recently studied
 51 the interplanetary conditions leading to large geomagnetic storms as detected in the *Dst* index and
 52 found $\tau \approx 6$ hrs (with a 2σ uncertainty range of 4-12 hrs) was optimum for predicting the maximum
 53 of the storm (i.e., the minimum *Dst*) but $\tau \approx 4.5$ days was needed to best predict the integrated *Dst*
 54 over the duration of the storm. Paper 1 [*Lockwood et al.*, 2018b] studied energy coupling from the

55 solar wind into the magnetosphere and showed that neglecting the effects of gaps in interplanetary
 56 data has, in the past, introduced serious errors into derived solar wind-magnetosphere coupling
 57 functions. Paper 1 also used near-continuous data to show that there is no evidence that the
 58 coupling function varies with averaging timescale τ between 1 minute and 1 year. Paper 2
 59 [Lockwood *et al.*, 2018c] used this result to study the distribution of power input into the
 60 magnetosphere P_α and why the probability density function (p.d.f.) of $\langle P_\alpha \rangle_\tau$ (i.e., P_α averaged over
 61 intervals of duration τ) has the form it does at $\tau = 1$ min. Paper 2 also showed how this p.d.f.
 62 evolves with increasing τ up to 3 hours, giving the observed p.d.f.s of 3-hourly geomagnetic
 63 indices. In the present paper, we study how the distributions of power input into the
 64 magnetosphere, and of the geomagnetic indices, continue to evolve with increasing τ between 3
 65 hours and 1 year, allowing us to study the relationships of the p.d.f. at any relevant τ to the annual
 66 mean. These are key relationships that can make it possible to construct a climatology of space
 67 weather events based on observations of solar variability over the past 400 years.

68 **1.1 Core distributions of space weather variables and extreme events**

69 In this section, we make clear the distinctions between the “core” distribution of space weather
 70 events, “large events” (for example, Lockwood *et al.* [2017a; 2018a] studied events in the top 5%)
 71 and “extreme events”. Our aim is to investigate how much information on the extreme events
 72 could potentially be gleaned from the annual means and the core distribution. We use the 3-hourly
 73 *ap* planetary geomagnetic range index which are available continuously since 1932. This index is
 74 used because of the longevity of the data series and because it is more robust than the *aa* index as it
 75 employs more than just two observatories. Appendix B shows that the *ap* index has a marked
 76 tendency to exaggerate the semi-annual variation in average values by having a larger response to
 77 events occurring at the equinoxes and also has a lower response to large events during northern-
 78 hemisphere winter. We here use a version of *ap*, *ap_C*, that includes a correction for the effect of
 79 this uneven response in *ap*, as described in Appendix B. To compare to any events before 1932 we
 80 use the *aa* geomagnetic index, using inter-calibration curves that are also presented in Appendix B.
 81 Allen [1982] pointed out that averages of *ap* over a calendar day (by convention referred to as $Ap =$
 82 $\langle ap \rangle_{\tau=1\text{day}}$) are not appropriate for defining storm days because an isolated storm that spans
 83 midnight UT would be recorded as two moderately disturbed days rather than a single large storm

84 day. Hence *Allen* proposed using 24-hour boxcar (running) means of ap , which he termed Ap^* .
85 These have been employed by *Kappenman*, [2005] and *Cliver and Svalgaard* [2004]. For the
86 purposes of identifying and ranking storm days we take the largest value of the 8 such running-
87 means of the corrected ap index in each calendar day, $[Ap_C^*]_{MAX}$. A rank-order listing of the
88 largest events defined this way is given in the Supporting Information file, along with available
89 references.

90 Many papers have found variables of near-Earth interplanetary space and the magnetosphere
91 approximately follow a lognormal (or similar) distribution for the great majority of the time
92 [*Hapgood et al.*, 1991; *Dmitriev et al.*, 2009, *Vaselovsky et al.*, 2010; *Farrugia et al.*, 2012;
93 *Lockwood and Wild*, 1993, *Weigel and Baker*, 2003; *Vörös et al.*, 2015, *Love et al.*, 2015; *Lotz and*
94 *Danskin*, 2017; *Riley and Love*, 2017, *Xiang and Qu*, 2018]. This mathematical formulation
95 describes the “core” of the distribution, but often fails to match the occurrence of very large or
96 extreme events [e.g., *Riley*, 2012; *Baker et al.*, 2013, *Cliver and Dietrich*, 2013; *Lotz and Danskin*,
97 2017]. Hence such cases are often described by substituting a distribution to the large-event tail
98 that is different to that which fits the core of the distribution. Extreme Value Statistics (EVS) [e.g.,
99 *Kotz and Nadarajah* 2000; *Beirlant et al.* 2004; *Coles*, 2004] has been widely applied, initially in
100 studies of hydrology but subsequently to extreme terrestrial weather events and many other areas
101 such as in engineering, insurance and finance. The “extremal types theorem” (also called the
102 “Fisher–Tippett–Gnedenko” theorem) [*Coles*, 2004], states that extreme maxima follow one of
103 three types of distribution (“Gumbel”, “Fréchet” and “(negative) Weibull”, which are encapsulated
104 in a family of continuous probability distributions called the Generalized Extreme Value (GEV)
105 distribution. In the “block maxima” (BM) approach to extreme values, the observation period is
106 divided into non-overlapping periods of equal size and attention given to the maximum observation
107 in each period to which the GEV distribution applies. In the “peaks-over-threshold” (POT)
108 approach, observations that exceed a certain high threshold are selected. The second theorem in
109 extreme value theory is the Pickands–Balkema–de Haan theorem and states that the threshold
110 excesses have an approximate distribution within the “Generalized Pareto Distribution” (GPD)
111 family. EVS has been applied to geomagnetic indices (for example by *Siscoe* [1976], *Tsubouchi*
112 *and Omura*, [2007], *Silbergleit* [1996; 1999], *Chapman et al.* [2018] and *Mourenas et al.* [2018]),
113 to the occurrence of very large Geomagnetically-Induced Currents (GICs) [*Thompson et al.*, 2011;

114 *Lotz and Danskin, 2017*], and to the fluxes of energetic magnetospheric particles [*Koons, 2001*;
 115 *O'Brien et al., 2007*].

116 Figure 1 places into context the relationship of the extreme event tail to the core distribution for
 117 geomagnetic activity as measured by the (corrected) ap index, ap_C . The plot shows (top) some
 118 selected annual distributions of the Ap_C^* index and (bottom) the corresponding distributions of
 119 Ap_C^* as ratio of the annual mean value, $Ap_C^*/\langle ap_C \rangle_{\tau=1yr}$. The gray histograms are for all available
 120 Ap_C^* data (i.e. covering the years 1932-2016). Note that we here quote ap , and hence ap_C , Ap_C^*
 121 and $[Ap_C^*]_{MAX}$, as indices without units (the standard ap values are an index in units of 2nT and
 122 hence the values in nT would be double those given here [*Menvielle and Berthelier, 1991*]). The
 123 black vertical dashed line shows Apo , the 95th percentile of all available samples. The year 1960
 124 (shown in red) was one year after the maximum of the largest sunspot cycle (number 9) of the
 125 recent grand solar maximum [*Lockwood et al., 2009*] and gave the largest annual mean value since
 126 ap measurements began ($\langle ap_C \rangle_{\tau=1yr} = 23.65$) and also contained the largest observed event since
 127 1932, as determined by a daily $[Ap_C^*]_{MAX}$ value of 249 on 13 November of that year. The year
 128 2009 (in blue) was at the low sunspot minimum (between cycles 23 and 24) gave the smallest
 129 annual mean in the record ($\langle ap_C \rangle_{\tau=1yr} = 3.93$). The year 1859 (in orange) has been chosen because
 130 between 28 August and 5 September of that year, the Carrington event took place (see
 131 contemporary reports by E. Loomis, collected together by *Shea and Smart [2006]*), which is
 132 thought to be the largest terrestrial space weather event to have been observed as it happened
 133 [*Nevanlinna, 2006; Cliver and Dietrich, 2013; Ngwira et al., 2014*]. The mean $\langle ap \rangle_{\tau=1yr}$ for 1859
 134 has been estimated to have been 10.98 by *Lockwood et al. [2018a]*. The distribution of daily Ap
 135 occurrence for 1859 shown in Figure 1 has been generated from the estimated mean value for that
 136 year using a model that will be developed in the present paper and is described in Appendix A. The
 137 distribution for 2012 is included (in green, $\langle ap_C \rangle_{\tau=1yr} = 9.20$) because on 23 July of that year a
 138 very large and very rapid Coronal Mass Ejection (CME) erupted, an event which would have
 139 generated extreme terrestrial space weather (a “superstorm”) had it hit the Earth. It was observed as
 140 it passed over the STEREO-A spacecraft and, from modelling based on the measurements taken by
 141 that craft and by solar instruments, it is estimated it would have caused a terrestrial event as large as
 142 the Carrington event, had the eruption taken place just one week earlier such that the CME would
 143 have hit Earth’s magnetosphere instead of STEREO-A [*Baker et al., 2013; Ngwira et al., 2013*].

144 From available magnetometer data, *Nevanlinna* [2006] has estimated that the daily *aa* geomagnetic
 145 index reached $Aa = 400\text{nT}$ during the Carrington event. This estimate allows for missing data, but
 146 may still be an under-estimate and *Cliver and Svalgaard* [2004] estimated the peak value of the
 147 running mean of a corrected version of the *aa* index over 24 hours of Aa^* to be 425nT . The *aa*
 148 index was designed by *Mayaud* [1972, 1980] to act as an equivalent to the *ap* index using data from
 149 just two stations: however, the data since 1932 show that the two are not linearly related, with *ap* at
 150 large *aa* being significantly lower than would be obtained from a linear fit. Polynomial fits of daily
 151 means, Ap , as a function of the daily means in *aa* (by convention termed Aa) are given in Appendix
 152 B for the four quarter-year intervals around the equinoxes and solstices. Taking the peak Aa to be
 153 425nT for the Carrington event, the relevant equation (B3) gives an estimated maximum Ap^* value
 154 of 284 ± 30 . Because it is considered that the STEREO event would have given a storm comparable
 155 to the Carrington event, we here take this Ap^* to apply to it as well. These values of $[Ap^*]_{\text{MAX}}$ of
 156 284 are shown by the vertical dot-dash lines. Applying the time-of-year correction given in
 157 Appendix B, this yields $[Ap_C^*]_{\text{MAX}}$ of 215 ± 23 and 211 ± 23 , respectively, for these two events.
 158 These estimated $[Ap_C^*]_{\text{MAX}}$ values for the Carrington and STEREO events are shown in Figure 1a
 159 by, respectively, the solid vertical orange and green vertical lines. By way of comparison, the
 160 largest daily-mean in the observed $[Ap_C^*]_{\text{MAX}}$ record (since 1932) is 249, recorded on 13 November
 161 1960.

162 The list of storm days, since 1932 ranked by their $[Ap_C^*]_{\text{MAX}}$ values is given in the Supporting
 163 Information file. It has similarities to other such lists [e.g., *Nevanlinna et al.*, 2006; *Kappenman*,
 164 2005; *Cliver and Svalgaard*, 2004], but there are differences because we have made allowance for
 165 the variation with time-of-year of the Ap^* response and, in the case of the Carrington event, the
 166 relationship between the Aa^* and Ap^* indices. Even quite small changes in the estimated
 167 magnitude of the storm day can have a large effect on its ranking order. The major surprise is that
 168 the positions of both the Carrington and STEREO events in the list is somewhat lower than in other
 169 lists if we correct for the time-of-year dependence of ap (estimate 1, $[Ap_C^*]_{\text{MAX}}$). This raises the
 170 question as to whether this correction should be applied to these events or not. Logically, there is no
 171 doubt that it should be as equation B-3 converts the Aa^* estimate into an Ap^* value which should
 172 then need correcting to become Ap_C^* . The main argument for not applying the correction is that the
 173 original Aa^* estimate is a proxy compiled from other sources. That these sources are largely

174 European-sector mid-latitude observatories and Ap is heavily weighted to mid-latitude European
 175 station data, does argue that this correction should indeed be applied. However, there remains
 176 great uncertainty in the true magnitude of the Carrington event. We also note that $[Ap_C^*]_{MAX}$ is
 177 almost certainly not a fully adequate metric of this superstorms because it does not take account of
 178 the fact that the Carrington event on 3 September was in the middle of an extended interval of very
 179 high geomagnetic activity between 28 August and 5 September and this almost certainly drove
 180 excessively large negative Dst values through the integrated effect on the ring current population,
 181 giving the famously large negative deflection recorded at the lower-latitude Colaba observatory in
 182 Mumbai.

183 *Lockwood et al.* [2017a] estimated the annual mean power input into the magnetosphere $\langle P_\alpha \rangle_\tau$
 184 from the reconstructed solar wind and interplanetary field variables derived by *Owens et al.* [2017],
 185 and from this *Lockwood et al.* [2018] have estimated that the annual mean of ap for 1859 was
 186 10.98. Hence the estimated peak $[Ap_C^*]_{MAX} / \langle ap_C \rangle_{\tau=1yr}$ for the Carrington event is 19.5 ± 2.1
 187 (shown by the solid orange line in the lower panel of Figure 1) for the corrected data and
 188 $[Ap^*]_{MAX} / \langle ap_C \rangle_{\tau=1yr} = 25.9 \pm 2.7$ for the uncorrected value (the orange dot-dashed line). From the
 189 observed $\langle ap_C \rangle_{\tau=1yr}$ of 9.20 for 2012 the $[Ap_C^*]_{MAX} / \langle ap_C \rangle_{\tau=1yr}$ for the STEREO event would have
 190 been 23.0 ± 2.5 (shown by the green line in the lower panel of Figure 1) and $[Ap^*]_{MAX} / \langle ap_C \rangle_{\tau=1yr} =$
 191 30.9 ± 3.3 for the uncorrected data (green dot-dash line). These ratio estimates are much larger
 192 values than for the observed 13 November 1960 event, for which $[Ap_C^*]_{MAX} / \langle ap_C \rangle_{\tau=1yr}$ is
 193 considerably lower, being 10.51 because it occurred during the most active geomagnetic year on
 194 record. Table S-7 of the Supporting Information shows that the largest value of
 195 $[Ap_C^*]_{MAX} / \langle ap_C \rangle_{\tau=1yr}$ in the observational record (since 1932) is 16.27 for 8 February 1986 (for
 196 which $[Ap_C^*]_{MAX} = 203$, the 7th largest value). This is the outstanding example in the observational
 197 record of a big storm being observed very close to sunspot minimum; however, its
 198 $[Ap_C^*]_{MAX} / \langle ap_C \rangle_{\tau=1yr}$ ratio is still very much smaller than that estimated for the Carrington and
 199 STEREO events. In their absolute corrected Ap_C^* values or uncorrected Ap^* values, the Carrington
 200 and STEREO events appear to be comparable with, or somewhat larger than, the largest events seen
 201 since 1932; however, they arose in years of relatively low average activity and so are wholly
 202 exceptional in their $Ap_C^* / \langle ap_C \rangle_{\tau=1yr}$ and $Ap^* / \langle ap_C \rangle_{\tau=1yr}$ values.

203 Figure 1 demonstrates why the description of superstorms requires more than an extrapolation of
204 the core and hence needs the application of EVS. However, there may still some valuable
205 information on extreme events to be obtained from the core distribution, as *Love* [2012] and *Love et*
206 *al.* [2015] have demonstrated for large geomagnetic storms (as defined and quantified using the *Dst*
207 geomagnetic index). The points in Figure 2 show the available 31040 24-hour $[Ap_C^*]_{MAX}$ samples
208 as a function of the annual mean of the year in which they occur: the cyan points are the top 100
209 days (0.32%) in terms of $[Ap_C^*]_{MAX}$ value (shown by the short vertical cyan lines in Figure 1); the
210 mauve points are the top 6 days (0.02%, shown by the short vertical mauve lines in Figure 1); and
211 the grey points are the remaining 99.68%. Figure 2 stresses how much our understanding rests
212 rather critically on the estimates of the 1859 and 2012 superstorm values of (the orange and green
213 squares being the uncorrected values and the triangles being the corresponding corrected values).
214 If we do not consider these two events and look just at the observed record since 1932, we see a
215 quite strong relationship between the largest value seen in the year and the average value for that
216 the year with the data points falling in the bottom right half of the plot. The corrected $[Ap_C^*]_{MAX}$
217 values for the 1859 and 2012 superstorms (the orange and green triangles) are close to being in line
218 with this relationship, especially the lower values of the uncertainty range. These values suggest
219 that the occurrence of extreme superstorms is (weakly) related to the average activity in those years
220 and that the extreme events are forming something like the negative Weibull distribution “pile up”
221 towards a maximum possible value not much greater than that for the November 1960 event.
222 However the uncorrected values, $[Ap^*]_{MAX}$ (shown by the green and orange squares) appear to be a
223 completely different class of event from the events seen after 1932 and not obeying any sort of
224 relationship between the peak and mean values. We should here also note that it is possible that
225 even these uncorrected values are underestimates (being based on the *Cliver and Svalgaard* [2004]
226 estimate of Aa^*) that have been limited by procedure of quantizing the available data into k-index
227 bands [see *Lockwood et al.*, 2018d]. Thus the uncertainty in the estimated severity of the
228 Carrington and STEREO events becomes crucial. On the other hand, the lower estimates for the
229 Carrington and STEREO events suggest that the annual mean value and the core distribution could
230 be helpful in quantifying the probability of the extreme events.

231 Even if the former proves to be the case and annual means or of no assistance in predicting
232 superstorms, characterizing the core of the distribution (as opposed to the extreme tail) is, however,
233 still important in space weather applications where the integral of the space weather activity is of

234 relevance and the threshold to the effect is not in the extreme tail. Examples would include the
235 effect of GICs on pipeline corrosion [Boteler, 2000; Pulkkinen et al., 2001; Gummow, 2002; Cole,
236 2003; Pirjola, 2005; Pirjola et al., 2005, Viljanen et al., 2006; Ingham and Rodger, 2018]; the
237 effect of GICs on power grid transformer degradation [Kappenman, and Radasky, 2005; Gaunt,
238 2016]; the effect of energy deposition in the upper atmosphere on the orbits of LEO satellites and
239 space debris [Doornbos and Klinkrad, 2006]; and the effect of integrated radiation dose on the
240 degradation of spacecraft electronics [Baker, 2000; Fleetwood et al., 2000]. In all these examples,
241 although the extreme superstorm events have a large effect, they are rare and a much larger number
242 of smaller events, described by the core distribution, can also have a significant integrated effect.
243 Lastly, we note that Chapman et al. [2018] have recently studied the extreme event tails in several
244 terrestrial disturbance indices during recent maxima of the solar cycle and fitted Generalized Pareto
245 Distributions. They found that if the mean and variance of the large-to-extreme observations can be
246 predicted for a given solar maximum, then a relationship between the core distribution and the
247 extreme tail can be found giving a description of the full distribution. Thus it does appear possible
248 that the study of the core of the distributions presented here could be extended to characterize the
249 extreme tails: this will be the subject of a future study.

250 As mentioned above, the $[Ap_C^*]_{MAX}$ values are unlikely be the best indicators of all storm
251 characteristics, in particular in relation to the ring current and the *Dst* geomagnetic index. This
252 gives another reason why we should study the core of the distributions, associated with storm “pre-
253 conditioning” and the fact that the best predictors of large *Dst* storm occurrence are time-integrated
254 over long intervals (several days) [Lockwood et al., 2016; Borovsky, 2017]. The largest and most
255 disruptive geomagnetic storms tend to be the longest lived [Balan et al., 2016; Echer et al., 2008;
256 Mourenas et al., 2018]. Many large and long-lived storms show a “two-step” development
257 [Tsurutani et al., 1999; Xie et al., 2006]; however, these multistep storms have been shown not
258 originate from just a simple superposition of individual events [Chen et al., 2000; Kozyra et al.,
259 1998, 2002] and it is not yet fully clear how the implied pre-conditioning originates. Kozyra et al.
260 [1998] argued that prior energetic particle injections are swept out of the dayside magnetopause as
261 the second population from the plasma sheet moves into the inner magnetosphere and so suggested
262 that the preconditioning occurs in a multistep storm through the cumulative effects of the
263 successive storms on the population in the source plasma sheet [Chen et al., 2000; Kozyra et al.,
264 1998, 2002]. Alternatively, it has been suggested that prior storms prime the inner magnetosphere

265 through O⁺ ions injected from the ionosphere [*Hamilton et al.*, 1988; *Daglis*, 1997]. *Lockwood et*
266 *al.* [2016] have shown that the key element in driving the largest storms (as measured by the *Dst*
267 index) is not so much the peak magnitude of the interplanetary coupling function, rather the
268 timescale over which it applies – large storms being a response to forcing that is both large and
269 sustained over several days. (In other words, very large interplanetary coupling function values do
270 not drive major storms if they persist for only short intervals). *Borovsky* (2016) reached the same
271 conclusion in relation to the damaging relativistic electron fluxes generated in the largest storms.
272 Thus there is likely to be some information in the core of the distributions that could be exploited to
273 predict the occurrence of the long-lived and extreme events. Lastly, we also note that *Kauristie et*
274 *al.* [2017] have also looked at the core distributions of *ap*, *Dst* (as well as *am* and *dDst/dt*), not with
275 a view to identifying highly disturbed periods and large and extreme events, rather the opposite - to
276 find the quietest intervals that could be used to generate an empirical model of the undisturbed main
277 field.

278 **1.2 Construction of a Space-Weather Climatology**

279 A number of techniques that have been developed and refined for terrestrial meteorological and
280 climate studies are now being deployed in the field of space weather. In addition to EVS discussed
281 above, these include: NWP (Numerical Weather Prediction) [*Pizzo et al.*, 2015]; DA (Data
282 Assimilation) [*Siscoe and Solomon*, 2006; *Schunk et al.*, 2014; *Barnard et al.*, 2017; *Lang*, 2017];
283 cost-loss analysis [*Owens and Riley*, 2017]; ensemble forecasts [*Knipp*, 2016]; climate analogue
284 forecasts [*Barnard et al.*, 2011]; ensemble climate reconstructions [*Owens et al.*, 2016a; b], skill
285 scores [*Balch*, 2008]; cost-loss analysis [*Henley and Pope*, 2017]; and several others. In
286 meteorology, many of these techniques are used in conjunction with a “climatology” which
287 describes statistically the probability of a relevant variable at key locations having one of the full
288 potential range of values. “Climatological forecasts” assume that the future of a system can be
289 determined from these statistical properties of the past behavior of that system. These will clearly
290 often be rendered invalid by long-term changes in the system that are not covered by the
291 climatology. This limitation to climatological forecasts can actually be useful because deviations
292 from climatological forecasts (“anomalies”) can be used to detect and quantify the effects of the
293 long-term changes. Note that long-term changes can also generate false conclusions about, for
294 example, skill scores or event occurrence, if they are neglected [e.g., *Hamill and Juras*, 2006].

295 There are four elements that we need to generate a useful climatology of space weather for each of
296 the key variables: (1) the mean value (over a convenient period such as a year); (2) the core
297 distribution of values about that mean; (3) the extreme tail of the distribution (giving the repeat
298 period of superstorms); and (4) the autocorrelation function, ACF. All these would be available to
299 us, if we possessed the time series at high enough temporal resolution and over an interval long
300 enough that adding any more data does not significantly alter the distribution. This approach has
301 been employed by *Matthes et al.* [2017] to build a space climatology using the *aa* index
302 geomagnetic that extends back to 1868. Unfortunately, as discussed below, this does not include
303 the grand minima conditions such as existed during the Maunder minimum [*Usoskin et al.*, 2015]
304 that we know from cosmogenic isotopes to have prevailed for extended periods roughly 30 times in
305 the last 9000 years [e.g., *Barnard et al.*, 2011]. These four elements would enable us to evaluate
306 integrated deterioration of systems influenced by space weather, the probability of an event over a
307 certain size and the probability of multiple events that may have a greater effect than the sum of the
308 effect of the events individually. There is great emphasis in space weather on protecting systems
309 from the largest events or, at least, evaluating the risk posed by those events. However, evaluating
310 the distribution core and mean and the probabilities of quiet conditions is also important to avoid
311 the cost and other wasted resources associated with “over-engineering” systems (such that they
312 become obsolete long before they are lost or degraded) and so ensuring that the designs are cost-
313 effective. As pointed out by *Henley and Pope* [2017], the development of a useful space weather
314 climatology, as with forecasting procedures, requires a detailed dialogue with the system design
315 engineers and end-users.

316 The biggest problem in trying to assemble a space-weather climatology is the long timescales of the
317 variations [*Henley and Pope*, 2017]. The primary periodicity in space weather is the solar cycle
318 oscillation the period of which averages about 11 years. Since *in-situ* observations of the near-Earth
319 space environment began, we have accrued direct space-weather data for just four such cycles. To
320 put this in context, consider a terrestrial tropospheric weather climatology: the dominant periodicity
321 is one year and a climatology based on just four years would not be of much value for most
322 applications. Hence, as pointed out by *Lockwood* [2003], we need to extend the interval by using
323 other measurements and inferring the space weather variables, rather than just using the directly
324 measurements.

325 The most direct way of doing this is to employ geomagnetic activity observations, as used by
326 *Matthes et al.* [2017]. In theory these could extend back to 1832, when Gauss established the first
327 well-calibrated geomagnetic observatory in Göttingen. Reviews of the development of the
328 observation of geomagnetic activity have been given by *Stern* [2002] and *Lockwood* [2013]. Some
329 composites have used geomagnetic activity data from soon after the establishment of Gauss'
330 observatory; for example, *Svalgaard and Cliver* [2010] used regressions with different types of
331 geomagnetic data to extend the sequence back to 1835. However, there are concerns about the
332 calibration, stability and homogeneity of the earliest data [*Lockwood*, 2013].

333 Geomagnetic activity on annual timescales depends on both the solar wind speed V_{SW} and the IMF
334 field strength, B , and the first separation of the two was made by *Lockwood et al.* [1999] using two
335 different geomagnetic indices (the aa index and Sargent's recurrence index derived from aa). Later,
336 *Lockwood* [2014] used 4 different pairings of different indices to derive V_{SW} , B and the open solar
337 flux, with a full Monte-Carlo uncertainty analysis, back to 1845. From this date, the geomagnetic
338 data give us almost 17 full solar cycles, considerably more useful than the 4 available in direct
339 observations but still not enough for a full climatology that allows for centennial scale solar change.
340 Crucially, this interval does not include the Maunder minimum (or even the lesser Dalton
341 minimum) and hence a climatology based on geomagnetic data would not cover grand minimum
342 conditions or even periods like the Dalton minimum.

343 Recent advances allow us to start to construct a climatology based on sunspot numbers which are
344 available with reasonable regularity from about 1612, soon after the invention and patenting of the
345 telescope in 1608. *Owens et al.* [2017] have used the sunspot number data in conjunction with
346 modelling to reconstruct the solar wind number flux N_{SW} , as well as B and V_{SW} from 1615 onwards.
347 This has enabled *Lockwood et al.* [2017] to reconstruct the annual mean power input into the
348 magnetosphere from 1615 and from this *Lockwood et al.* [2018a] have estimated the annual means
349 of the ap index. These advances make it possible to construct elements of a climatology which
350 extends over 30 clear solar cycles as well as the 50-year break to normal solar cycles during the
351 Maunder minimum. During the Maunder minimum, the modelling predicts 8 small-amplitude,
352 smaller-period cycles which show a different phase relationship with the weak cycles in sunspot
353 numbers. *Owens et al.* [2012] have shown evidence for these small Maunder-minimum cycles in
354 galactic cosmic ray fluxes.

355 In addition to the increased number of solar cycles, these reconstructions that extend back to the
 356 early 17th century cover both a grand minimum (the Maunder minimum [*Usoskin et al.*, 2015]) and
 357 the recent grand solar maximum [*Lockwood et al.*, 2009]. There is also potential to even extend the
 358 climatology to cover up to 9000 years, covering 24 grand maxima and 30 grand minima, using
 359 cosmogenic isotope abundance measurements which generally require decadal averages or which
 360 are smoothed by the time constants of the isotope deposition into the terrestrial reservoirs where
 361 they are measured. *Barnard et al.* [2011] have discussed a method for temporal scale-changing
 362 from these decadal-scale data to annual means. At the present time we are lacking one key element,
 363 namely a way to determine the times of solar cycle minimum and/or maxima and hence the phase
 364 of the solar cycle of each year.

365 In paper 1 of this series of 3 papers [*Lockwood et al.*, 2018b], we showed that the total power input
 366 into the magnetosphere P_α can be computed using a constant coupling exponent α that does not
 367 depend on the averaging timescale τ (previous studies that had suggested it did were adversely
 368 influenced by data gaps). Paper 2 [*Lockwood et al.*, 2018c] studied how the core distributions of P_α
 369 on timescales of 3 hours and less arise. In the current paper we study how and why these
 370 distributions in P_α evolve with averaging timescale τ and the subsequent evolution with τ of the *ap*
 371 (section 2) and *Dst* (section 3) geomagnetic indices. In each of these two sections we develop an
 372 algorithm that allows the core distribution for that geomagnetic index to be evaluated for a given
 373 mean value and at a required timescale, τ . The formulae required to implement these algorithms are
 374 given in Appendix A.

375 **2. Distributions of power input to the magnetosphere and geomagnetic indices**

376 Figure 3 studies the evolution with averaging timescale τ of the distribution of three space weather
 377 indicators. The left-hand panels show the power input into the magnetosphere, computed from the
 378 near-continuous interplanetary data for 1996-2016 (inclusive) and normalized to the mean value
 379 over the calendar year, $\langle P_\alpha \rangle_\tau / \langle P_\alpha \rangle_{1\text{yr}}$. The central panels show the normalized geomagnetic *ap*
 380 index, $\langle ap \rangle_\tau / \langle ap \rangle_{1\text{yr}}$ from the full dataset available (for 1932-2016) and the right-hand panels how
 381 the normalized negative geomagnetic *Dst* index, $\langle Dst' \rangle_\tau / \langle Dst \rangle_{1\text{yr}}$, (where *Dst'* is defined below),
 382 again using all the available data (for 1957-2016).

383 The coupling function of $\alpha = 0.44$, shown in Paper 1 [Lockwood *et al.*, 2018b] to apply at all τ , is
384 used with the equation of Vasylunas *et al.* [1982] to generate P_α [described in Lockwood *et al.*,
385 2017, 2018a;b]. The ap index responds primarily to the substorm current wedge [see Lockwood,
386 2013] and the Dst index primarily to the ring current. However, Dst is importantly also influenced
387 by other currents [e.g. Turner *et al.*, 2000] such as the Chapman-Ferraro currents in the
388 magnetopause and so also varies with compressions of the dayside magnetosphere by solar wind
389 dynamic pressure enhancements. The ring current effect dominates meaning that Dst is
390 increasingly negative as activity increases but the dynamic pressure effect mean that positive Dst
391 value can occur. Corrections for the effect of solar wind dynamic pressure on Dst , via
392 magnetopause currents, have been developed [O'Brien and McPherron, 2000; Consolini *et al.*,
393 2008] but we do not use them here, mainly because it reduces the available dataset to after 1996
394 (when quasi-continuous interplanetary data are available) but also because a great many papers
395 have used the uncorrected Dst index to characterize magnetic storms in the past. The fact that Dst ,
396 unlike ap (or P_α), can have either sign generates a fundamental difference between the ap and Dst
397 indices when trying to formulate a long-term climatology: when activity is low ap tends to a
398 limiting value of zero whereas Dst tends towards a distribution of values spread around zero. Half-
399 wave rectifying Dst so that positive values are put to zero is not an option as this generates a large
400 number of samples at zero that distorts the distribution. Instead we here treat $Dst \geq 0$ as data gaps
401 (we here call the index so derived Dst') which yields an index that correlates much better with
402 multiplicative interplanetary coupling functions [Lockwood, 2013]. However, such samples are still
403 included in the total number when computing the occurrence probability of a large negative Dst
404 value. Note that using Dst' instead of Dst is purely a measure that gives us a unipolar activity index
405 to work with (which makes the modeling required much less complex) and is not, in any way, a
406 correction for magnetopause currents. Of course, even strongly negative Dst values will still be
407 influenced by magnetopause currents to some extent, which is why Dst is an imperfect metric of
408 ring current storms. In a later paper we will present a separate model for predicting the
409 distributions of the pressure-corrected index, Dst^* , as a function of τ . Note that Dst^* also has both
410 positive and negative values (see Figures 1 and 2 of Consolini *et al.* [2008]) and so the same sort of
411 techniques will be required for the construction of a model for Dst^* as are used here for Dst .

412 To summarize the procedure employed here: we make normalized values of the variable X , where X
 413 is one of the observed variables P_α , ap , and Dst for a given averaging timescale τ (also done for the
 414 synthesized variables X_R and X_{RF} that are used below to clarify the behavior of the observed
 415 variables). We normalise by dividing by the arithmetic mean for the calendar year of the sample
 416 $\langle X \rangle_{\tau=1\text{yr}}$. From these normalized values we derive the distribution of $X/\langle X \rangle_{\tau=1\text{yr}}$ for all 22 years
 417 studied. This distribution has an arithmetic mean $m = 1$ which is the “grand mean” or (the “mean-
 418 of-means”) of the 22 annual normalized data subsets and which applies because we have, to a good
 419 approximation, the same number of samples in each year. We then fit model p.d.f.s so that we can
 420 empirically model the probability of $X/\langle X \rangle_{\tau=1\text{yr}}$ which is the probability of X for a given $\langle X \rangle_{\tau=1\text{yr}}$,
 421 i.e. $P(X | \langle X \rangle_{\tau=1\text{yr}})$. Hence this enables us to achieve our goal of empirically modelling the
 422 distribution of X for a given $\langle X \rangle_{\tau=1\text{yr}}$. We wish this fitted distribution to reproduce the observed
 423 one as closely as possible so we use model distributions of means of $\mu = m = 1$ and find the
 424 optimum variance ν using Maximum Likelihood Estimation. Some of the distributions fitted are
 425 described by shape and scale parameters instead of μ and ν and these are constrained so that μ is
 426 unity. The procedure is repeated for the full range of averaging timescales, τ .

427 The blue histograms in Figure 3 are the observed distributions, the black lines shows the best-fit
 428 lognormal distributions and the mauve lines are the best-fit Weibull distributions (both with mean
 429 value $\mu = 1$ in the cases of P_α and ap and $\mu = R_m(\tau)$ for Dst' (where R_m deviates from unity because
 430 in Dst' we treat each $\langle Dst \rangle_\tau \geq 0$ sample as a data gap: the factor $R_m(\tau)$ is discussed further later).
 431 The blue histograms were generated by counting the number of samples in 150 contiguous bins
 432 centered on on $k.x_{98}/100$, where k is varied between 0.5 and 149.5 in steps of 1 and x_{98} is the 98th
 433 percentile of the distribution. The numbers of samples n in each bin then normalized so that
 434 $\Sigma n(x_{98}/100)$ is unity. Fitting directly a distribution to these histograms gives results which, in general,
 435 depend on the bin width adopted [e.g., *Woody et al.*, 2016] and so we here fit distributions using
 436 Maximum Likelihood Estimation (MLE) which does not require prior binning of the data into bins
 437 of arbitrarily-chosen width. A basic description of MLE fitting, and of goodness of fit metrics (both
 438 absolute and relative) is given in the Supporting Information file. Plots of best-fit probability density
 439 functions (p.d.f.s) and cumulative distribution functions (c.d.f.s), and tables of best-fit distribution
 440 parameters and goodness of fit metrics are also given in the Supporting Information file for seven
 441 standard distribution forms: the normal (Gaussian) distribution, the Lognormal distribution, the

442 Weibull distribution; the Burr distribution, the Gamma distribution, the Log-logistic (Fisk)
 443 distribution, and the Rician distribution. For all these distributions the number of degrees of freedom
 444 is $d_f = 2$, except the Burr for which $d_f = 3$.

445 The top row in Figure 3 is for averaging timescale $\tau = 1$ yr and the rows beneath are, successively
 446 for τ of 0.5 year, 27 days, 7 days, 1 day and 3 hours (0.125 day). The omission of positive $\langle Dst \rangle_\tau$
 447 samples has no effect for $\tau = 1$ year (as all values are negative), but the number of Dst' samples is
 448 99.17%, 94.08%, 88.42%, 80.60%, and 78.48% of all Dst samples for τ of, respectively, 0.5 year,
 449 27 days, 7 days, 1 day and 6 hours. Because of the normalization, the distributions for $\tau = 1$ yr are,
 450 by definition, delta functions at unity. At general τ , the distributions for $\langle ap \rangle_\tau / \langle ap \rangle_{1\text{yr}}$ are always
 451 close to lognormal in form (the black lines) the variance increasing with decreasing τ (see
 452 Supporting Information file for goodness-of-fit evaluations). At the larger τ , the low variance
 453 lognormal distributions are essentially Gaussian in form. On the other hand, the Dst' distributions
 454 are equally well fitted by the Weibull, Gamma or Log-logistic families of distributions (see
 455 Supporting Information) and in Figure 3 we show the Weibull distributions (the mauve lines), again
 456 with variance increasing with decreasing τ . Note that for Dst' , significantly better fits could be
 457 obtained using a distribution with an extra degree of freedom, such as the Burr (see supporting
 458 information). The difference between ap and Dst' is caused by the flatter and broader distribution
 459 at small $\langle Dst' \rangle_\tau / \langle Dst \rangle_{1\text{yr}}$ values. The $\langle P_\alpha \rangle_\tau / \langle P_\alpha \rangle_{1\text{yr}}$ distributions are lognormal in form for τ
 460 greater than about 2 days, but at lower τ these distributions are increasingly Weibull-like in form.
 461 The origin of a Weibull form at low τ was discussed in Paper 2 [Lockwood *et al.*, 2018c] and is
 462 associated with the variability of the Interplanetary Magnetic Field (IMF) orientation factor on
 463 these timescales, via the quasi “half-wave rectification” effect of the southward component of the
 464 IMF on solar wind – magnetosphere coupling. Note that because of the smoothing effect of the
 465 magnetospheric energy storage/release system, the Weibull distribution of power input to the
 466 magnetosphere for small τ yields a log-normal distribution in power input on the timescales
 467 relevant to ap and hence in ap itself.

468 The evolution of the distributions shown by the different rows of Figure 3 reveal the “Central Limit
 469 Theorem” (hereafter CLT) in action [Heyde, 2006; Fischer, 2011; Wilks, 1995]. This states that
 470 when independent random variables are added, their properly normalized sum tends toward a

471 normal distribution. It applies in this context because the key operation in taking an average value
 472 is summation and because, as τ is increased in relation to the correlation timescale, an increasing
 473 fraction of the samples are independent.

474 **2.1. The evolution of the distributions with timescale for ap and $P\alpha$**

475 Figure 4 looks in more detail at the evolution of the distributions of $\langle P_\alpha \rangle_\tau / \langle P_\alpha \rangle_{1\text{yr}}$ (for $\alpha = 0.44$) as
 476 a function of the logarithm of the averaging interval. The upper plot shows the probability density
 477 function (pdf) color-coded as a function of $\log_{10}(\tau)$ and $\langle P_\alpha \rangle_\tau / \langle P_\alpha \rangle_{1\text{yr}}$ such that the distributions
 478 shown in the left-hand plots of Figure 3 are vertical slices of Figure 4. The blue line in the lower
 479 panel shows the corresponding variation of the distribution variance ν (also on a logarithmic scale).
 480 Figure 5 is the corresponding plot for $\langle ap \rangle_\tau / \langle ap \rangle_{1\text{yr}}$.

481 In the Supporting Information file, the distributions shown in Figure 3 are fitted with seven
 482 distribution forms, six of which are characterized by two parameters (either the mean, m , and
 483 variance, ν , or a pair of parameters that are defined by m and ν). (Note the seventh distribution
 484 form used, the Burr, has an additional shape parameter and is included to test if this gives a
 485 statistically significant improvement to the fit). Two of the distributions, the Gaussian and the
 486 Rician, do not give good fits at low τ but do quantify the evolution of the distributions towards a
 487 Gaussian-like form as τ is increased towards 1 year. Because we here look at the distributions of
 488 normalized disturbance metrics $\langle X \rangle_\tau / \langle X \rangle_{1\text{yr}}$ (in this paper we consider X of P_α , ap and Dst) the
 489 mean m is, by definition, always unity and hence we only need to study the behavior of the
 490 variance, ν , shown in Figure 4b for $\langle P_\alpha \rangle_\tau / \langle P_\alpha \rangle_{1\text{yr}}$ and in Figure 5b for $\langle ap \rangle_\tau / \langle ap \rangle_{1\text{yr}}$.

491 **2.2. The effect of autocorrelation on the evolution of distributions**

492 To help understand Figures 4 and 5, Figure 6 shows the evolution with increased τ for a synthesised
 493 variable X_R that is selected at random at time resolution $\tau = 3$ hrs from a Weibull distribution with
 494 k of 1.0625 and λ of 1.0240 (giving a mean $m = 1$) which in Paper 2 [Lockwood *et al.*, 2018c] was
 495 shown to be good fit to the distribution of $\langle P_\alpha \rangle_\tau / \langle P_\alpha \rangle_{1\text{yr}}$ at that timescale. The general pattern of
 496 evolution of the pdfs of $\langle X_R \rangle_\tau / \langle X_R \rangle_{1\text{yr}}$ in Figure 6a is like that in Figure 4a and 5a, other than that
 497 the distributions evolve towards a delta function at unity with increasing τ rather more rapidly for

498 X_R . This is also reflected by the mauve line in figure 6b, which shows that the variance, v , falls
 499 more rapidly than the blue and red lines in Figures 4b and 5b for P_α and ap , respectively. The initial
 500 distribution in Figure 6 is a Weibull form but even at τ as low as 9 hrs it has evolved into a
 501 lognormal form, which it keeps at all greater τ (but the variance falls so it approaches a Gaussian
 502 near $\tau = 1$ yr). This evolution of the distribution form is the same sequence that $P\alpha$ follows.

503 The mauve line in Figure 7 shows the autocorrelation function (the autocorrelation at lags of 3
 504 hours, the resolution of the synthetic data) of the random variable X_R employed in Figure 6. It can
 505 be seen that X_R is indeed completely random as the autocorrelation function falls to zero at lag 1. To
 506 investigate the effect of autocorrelation we generate a second random distribution which we then
 507 pass through a smoothing filter to give it autocorrelation. This generates a synthetic data series X_{Rf} .
 508 Because the filter has a similar effect on the distribution as averaging we have to draw the original
 509 random distribution from a higher-variance Weibull. By iteration we find that for the filter we use,
 510 an initial Weibull random distribution with k of 0.2800 and λ of 0.0778 (giving $m = 1$) generates an
 511 almost identical distribution at $\tau = 3$ hr after filtering to that of X_R used in Figure 6. The filter used is
 512 a triangular-weighting moving-average filter with two response peaks. The first is a [1-3-5-3-1],
 513 around lag $\delta t = 0$ which adds short-range correlation into the X_{Rf} data series. The second is a [1-2-3-
 514 4-5-6-7-8-7-6-5-4-3-2-1] $\times(5/8)$ triangular response peak centered on lag 216 (for the 3-hour
 515 resolution X_{Rf} data series, this second peak is at lag 27 day). The black line in Figure 7 shows the
 516 autocorrelation function of X_{Rf} and it can be seen that the filter has introduced short-term
 517 autocorrelation on lags up to about 1 day, and a 27-day (the mean solar rotation period seen from
 518 earth) recurrence.

519 Figure 8 shows the equivalent plot to Figure 6 for the X_{Rf} data series. Figure 8a shows that the
 520 effect of the autocorrelation is to slow the progression towards the delta function at unity. This is
 521 expected from the CLT because the autocorrelation means that larger averaging timescales are
 522 needed before samples are sufficiently uncorrelated for the CLT to apply. Figure 8b shows the
 523 variation of the variance v for X_{Rf} in black, and compares it with that for X_R (in mauve) from Figure
 524 6b. It can be seen that at the τ where autocorrelation has been introduced into the X_{Rf} series by the
 525 filter, the variance fall less quickly than for the random series, X_R . At all τ the distribution of X_{Rf} is
 526 lognormal in form and mirrors the evolution for ap . Note that Figures 7 and 8, and the results for a

527 random and a smoothed-random data series (X_R and X_{Rf}), are included here only to illustrate how
 528 autocorrelation influences the form of the evolution of the distribution with τ and also influences
 529 the dependence of variance ν on τ . They are not used again in the derivation of a model of the
 530 distribution at a given τ . Instead we fit the $\nu(\tau)$ variation derived directly from data with a
 531 polynomial in τ .

532 **2.3. Modelling the evolution of distribution of ap with increasing timescale**

533 The section describes how we model the evolutions of the distributions of $\langle ap \rangle_\tau / \langle ap \rangle_{1\text{yr}}$ with
 534 increasing τ and Figure 9a presents the results for that modelling, aimed at reproducing Figure 5a.
 535 Figure 9(b) shows the log-log plots of variance ν , as a function of τ from Figures 4b, 5b and 6b
 536 using the same color scheme, i.e. for P_a in blue, for ap in red and for the random variable, X_R in
 537 mauve. Also shown, in cyan, is the variation for the 150-year data series of the aa geomagnetic
 538 index. The black line is a polynomial fit to the ap variation, given by equations (A11) and (A12) of
 539 Appendix A which yield the variance, $\nu(\tau)$. The Maximum Likelihood analysis given in the
 540 Supporting Information (on which Figure 3 is based) shows that for $\langle ap \rangle_\tau / \langle ap \rangle_{1\text{yr}}$ the observed
 541 distribution at all τ is best fitted with a lognormal form with mean $m = 1$. (That is until τ approaches
 542 1 year when the distribution becomes nearly Gaussian in form and the goodness-of-fit metrics for
 543 all 7 distributions become very similar). Figure 9a shows the modelled lognormal distributions
 544 using the polynomial fit to the variance variation shown in Figure 9b. The equations for
 545 reproducing the distribution for a given τ are given in part (i) of Appendix A. From this, the p.d.f.
 546 of $\langle ap \rangle_\tau$ (and hence that of the time-integral of the activity $\tau \langle ap \rangle_\tau$) at a given τ can be computed
 547 for a known annual mean $\langle ap \rangle_{1\text{yr}}$.

548 The cyan line in Figure 9b is for all the full aa index data set which covers the interval 1868-2017.
 549 The close similarity of the $\nu(\tau)$ relationship to that for the ap data (1932-2017, the red line) strongly
 550 indicates that this relationship has not varied significantly over the past 150 years. To check this in
 551 more detail, the aa data have been divided into three 50-year intervals (1868-1917, 1918-1967 and
 552 1968-2017, inclusive), and the $\nu(\tau)$ relationship for these three data subsets are plotted in Figure

553 10b as green, blue and red lines, respectively, and can be seen to be very similar (and to that for the
 554 overall aa plot in Figure 9b). Figure 10a studies the autocorrelation function (ACF) of the
 555 $aa/\langle aa \rangle_{\tau=1\text{yr}}$ data for these three intervals. The three are again very similar showing the persistence
 556 effect at low τ (up to about 5 days), a recurrence peak at 27 days, plus some weak harmonics of the
 557 27 day variation, and hence are very similar to that for the smoother random variable, X_{RF} , in
 558 Figure 7. In fact, the ACF for X_{RF} could easily be made to match the observed ACFs for aa shown
 559 in figure 10 very closely, if the smoothing filter used were adjusted to give slightly lower
 560 persistence at low τ (< 1 day) and the response peak around 27 days were to be broadened
 561 somewhat. There is also a small but marked and persistent diurnal signal visible in Figure 10a.
 562 The main difference between the three intervals is that the 27-day peak is a little bit larger for the
 563 earliest interval (1868-1917) and the low- τ persistence a little bit weaker. These differences cannot
 564 be identified in the $\nu(\tau)$ plots. The only other data that are continuous and high enough time
 565 resolution to potentially investigate this further back in time are the daily values international
 566 sunspot number R , which are almost continuous since 1818. However, sunspot numbers behave
 567 very differently to geomagnetic activity indices, showing sudden increases/decreases as spot groups
 568 rotate onto onto/off the visible disk of the Sun and rises and falls as the groups wax or wane as they
 569 rotate across the visible solar disc: they do not have the bursty nature of Earth-directed
 570 interplanetary disturbances and hence of geomagnetic disturbances. Hence they cannot help us
 571 investigate the ACF, and the associated $\nu(\tau)$ relationship for near-Earth space and geomagnetic
 572 activity before the start of regular, well-calibrated geomagnetic observations.

573 Figure 11 investigates if ACFs and variances for aa shown in figure 10 vary with sunspot number.
 574 We use the international sunspot number R , derived and distributed by WDC-SILSO, Brussels. We
 575 take 3-year averages of the data to keep sample numbers high. For each period we evaluate the
 576 mean sunspot number, $\langle R \rangle_{\tau=3\text{yr}}$, and the ACF of $aa/\langle aa \rangle_{\tau=1\text{yr}}$. These ACFs were then averaged
 577 together for contiguous bins of $\langle R \rangle_{\tau=3\text{yr}}$ that are centred on values between 10 and 200 in steps of
 578 20. In addition the variance ν of the distribution of all $\langle aa \rangle_{\tau}/\langle aa \rangle_{\tau=1\text{yr}}$ samples in each band of
 579 $\langle R \rangle_{\tau=3\text{yr}}$ was computed for each averaging timescale τ . The top panel of Figure 12 shows a surface
 580 plot of the ACF as a function of $\log_{10}(\tau)$ and $\langle R \rangle_{\tau=3\text{yr}}$. On timescales below about $\tau = 25$ days the
 581 ACFs hardly varies at all with the sunspot number. The major effect is on the peak at 27 days (and
 582 its harmonics) which has a larger amplitude when the sunspot number is low. The lower panel gives

583 the corresponding surface plot of $\log_{10}(\nu)$: note that sample numbers do not allow this analysis to
 584 extend to as great a sunspot number as for the ACF analysis. As would be expected from the
 585 ACFs, there is almost no variation in the ν - τ relationship with sunspot number at τ below about 25
 586 days but above this the larger ACF peak at 27 days for low sunspot number causes ν to fall with τ
 587 slightly less rapidly than it does at higher sunspot numbers. There are some slight but persistent
 588 ridges and dips in the surface shown in figure 11b at certain $\langle R \rangle$ but the surface is remarkably
 589 independent of R . Note that the lack of any dependence of the ν - τ relationship on sunspot number
 590 (at low τ) was also revealed by Figure 8c of *Lockwood et al.* [2018a], which plots distributions of
 591 $\langle aa \rangle_{\tau=1\text{day}} / \langle aa \rangle_{\tau=1\text{yr}}$ as a function of year and no solar cycle variation can be detected.

592 It is tempting to argue that we should modify the model form of the ν - τ relationship at $\tau > 25$ days
 593 to allow for the (weak) sunspot number variation seen at large τ in the lower panel of Figure 12.
 594 The major reason is that during the Maunder minimum the persistently low sunspot number might
 595 make this a factor. However, this is not necessarily the case because a prolonged (grand) sunspot
 596 activity minimum is in many ways quite different to a sunspot activity minimum between solar
 597 cycles: one major reason being that for the cycle minima there is residual open flux generated
 598 during the previous cycle out of which fast solar wind flows. The 27-day ACF peak is largely
 599 caused by CIRs (Co-rotating Interaction Regions) caused by fast-solar wind emanating from
 600 coronal holes reaching down to low latitudes, catching up with Earth-bound slow solar wind of the
 601 streamer belt. Modelling for the Maunder minimum predicts that the streamer belt will have been
 602 considerably wider than in modern times with coronal holes restricted to high heliographic latitudes
 603 [*Lockwood and Owens, 2014a; b; Owens et al., 2017*], making CIRs that hit Earth less, rather than
 604 more, common. Hence it is not at all clear that that the effect noted in low sunspot years at $\tau > 25$
 605 days in Figure 12 will also apply to the Maunder minimum. For the present paper we assume that
 606 the $\nu(\tau)$ relationship does not change and we fit it with a single polynomial form. However, should
 607 a long-term changes in the $\nu(\tau)$ relationship be discovered at some point in the future, it could be
 608 readily accommodated by making the fit polynomial coefficients a function of time.

609 Figure 12 shows that the modelled distributions shown in Figure 9a can explain the variation of
 610 occurrence of large events, as a function of the annual means discussed in Paper 2. The points in
 611 Figure 12a show probability that 3-hourly values of ap are in the ap top 5% of the overall

612 distribution (for 1932-2016, 252152 samples), $f[ap > apo]$ (i.e., ap exceeds its 95-percentile of 3-
 613 hourly ap values, $apo = 47.91$), as a function of the annual mean value $\langle ap \rangle_{\tau=1\text{yr}}$. The mauve line is
 614 the prediction for $\tau=3\text{hrs}$ for the model values displayed in Figure 9a. The fit can be seen to be
 615 close. The family of model predictions of $f[ap > apo]$ as a function of $\langle ap \rangle_{\tau=1\text{yr}}$ is shown in Figure
 616 12b for timescales of 1 day (in blue), 7 days (in orange) and 27 days (in black). Hence the model is
 617 reproducing the behavior noted in Figure 1 of Paper 2, namely that, with some scatter, the number
 618 of events in any one year that are in the top 5% of the overall distribution, increases hyperbolically
 619 with the mean value for that year.

620 **2.4. The evolution of the distributions with timescale for Dst'**

621 Figure 13 is the equivalent plot to Figure 4 for the Dst' data which extend from 1957-2016. Here
 622 the pdf is shown as a function of τ and $\langle Dst' \rangle_{\tau} / \langle Dst \rangle_{1\text{yr}}$. Generating a model fit to this plot is
 623 more complex because Dst do not converge to zero for low activity and we have to use Dst'
 624 instead, where Dst' is the same as Dst , but all positive values are treated as data gaps. In annual
 625 mean data, this makes no difference, because all annual means are negative, but with decreasing τ
 626 the number of Dst' samples falls compared to the number of Dst samples, and the mean R_m of the
 627 distribution of $\langle Dst' \rangle_{\tau} / \langle Dst \rangle_{1\text{yr}}$, although unity at $\tau = 1$ year, is greater than unity at lower τ
 628 because negative values of $\langle Dst' \rangle_{\tau} / \langle Dst \rangle_{1\text{yr}}$ (i.e., positive values of $\langle Dst' \rangle_{\tau}$) are neglected.
 629 Figure 14a shows in red the variation with $\log_{10}(\tau)$ of $f_{\text{neg}} (= N_{Dst'} / N_{Dst})$, the fraction of Dst samples
 630 that are negative (the subset termed Dst'). The black line is a polynomial fit to this variation which
 631 is given by equation (A12) of appendix A. The green line shows the corresponding variation of R_m ,
 632 the mean of $\langle Dst' \rangle_{\tau} / \langle Dst \rangle_{1\text{yr}}$. Again the black line is best polynomial fit given by equation (A13)
 633 of Appendix A. Appendix A-ii gives the algorithm for computing the pdf of Dst' or a given Dst
 634 and timescale τ which allow for these two factors. Figure 15 corresponds to Figure 9 for the Dst
 635 index. As shown by Figure 3, the distributions of $\langle Dst' \rangle_{\tau} / \langle Dst \rangle_{1\text{yr}}$ follow the Weibull family of
 636 distributions and these are derived from the best fit to the observed $\log_{10}(v)$ - $\log_{10}(\tau)$ variation
 637 (shown in green in Figures 13b and 15b), using the polynomial fit given in black which is given by
 638 equations (A10) and (A11) of Appendix A. For comparison, Figure 15b also shows the $\log_{10}(v)$ -
 639 $\log_{10}(\tau)$ variations for P_a (in blue), ap (in red) and the random variable, X_R (in mauve).

640 Figure 16 corresponds to figure 12 and shows how the model can reproduce the occurrence of *Dst*
 641 below its 95 percentile value ($Dsto = -55.142\text{nT}$), as a function of the annual mean value. Figure
 642 16b shows the family of such variations for different values of τ .

643 3. Discussion and Conclusions

644 It is noticeable that the $\log_{10}(v)$ - $\log_{10}(\tau)$ variation for *ap* (in red in Figure 9b) flattens off as
 645 averaging timescale τ falls below about 1 day, whereas the variance v continues to rise with
 646 decreasing τ for power input into the magnetosphere, P_α (in blue). Using a synthesized random
 647 time series and a filter we have demonstrated how the flattening off is caused by autocorrelation in
 648 the time series. Hence there is autocorrelation in the *ap* time series at τ between 3hrs and 1day that
 649 is greater than that in P_α . As P_α is the driver of *ap*, this means that the geomagnetic response seen
 650 in *ap* is a smoothed response. This is not surprising, given the currents that the index is sensitive to
 651 and their associated time constants. The *ap* index is primarily influenced by the substorm current
 652 wedge [Lockwood, 2013] which is initiated only after a substorm growth phase lasting typically 30-
 653 40 minutes. Hence the rapid variations in the energy input into the magnetosphere, which are
 654 mainly associated with IMF orientation changes, are smoothed as energy (and open magnetic flux)
 655 are accumulated in the tail.

656 The same effect is even more clear for *Dst*, for which v flattens off as τ falls below about 3 days
 657 (the green line in Figure 15b which is again compared to the behavior for P_α in blue). Hence the
 658 smoothing effect on the response of *Dst* has a longer time constant than that for *ap*. The (negative)
 659 *Dst* index is responding primarily to the ring current [Turner *et al.*, 2000] which shows greater time
 660 constants, responding to the integral of solar wind forcing on timescales of order of a day or more
 661 [Lockwood *et al.*, 2016; Borovsky, 2016]. (Note that below we discuss the implications of the fact
 662 that even large negative *Dst* can be influenced by other factors, in particular, the magnetopause
 663 currents). This is not to say that P_α is the best coupling function explaining the solar wind influence
 664 on the ring current, not least because the coupling exponent α has been tuned to 0.44 to make P_α
 665 reproduce *ap*, not *Dst*. Nevertheless, the importance of southward IMF in driving disturbed *Dst*
 666 means that the same conclusions would be valid for any other coupling function that might better
 667 predict *Dst*.

668 Breaking down the power input into the magnetosphere P_α into its component factors, Paper 2
669 showed that the factors dependent on solar wind velocity and mass flux and on the IMF (F_V , F_N and
670 F_B) do not vary much on short timescales and the distribution of power input into the
671 magnetosphere is set by the variation in the IMF orientation factor F_θ which, although it can stay
672 stable for several days, is typically changing on minute timescales. Thus the shape of distribution is
673 set by F_θ , at very short timescales, much shorter than the timescale of the geomagnetic index
674 response – it then evolves with τ according to the CLT, making the shape of the distribution a
675 function of τ only.

676 A climatology is a statistical description that would enable us to evaluate the probability of space
677 weather events of a given magnitude and we are working toward one that applies to the full range
678 of solar conditions from grand solar minimum to grand solar maximum. In particular, there is value
679 in knowing the integrated level of activity over an extended period τ , which equals the average
680 value times the duration. Hence we investigate algorithms that can give us the probability of a
681 given average value for a given τ . These algorithms will be of great value in generating a long-term
682 climatology because they can compute the probabilities for a given annual mean and we have
683 annual means from the past 400 years from recent modelling work based on telescopic sunspot
684 observations [Owens et al., 2017]. The approach outlined in this paper is based on the finding that
685 the shape of the distribution of the normalized values (normalized by dividing by the annual mean
686 value) only depends on the averaging timescale τ . This was used by *Lockwood et al.* [2018a] to
687 look at the occurrence of “large” events (defined as in the top 5% since records began) over 400
688 years. The constancy of the shape of the distributions was just taken by *Lockwood et al.* [2018a] as
689 an empirical observation that could be exploited. The present series of three papers provide greater
690 understanding of why this empirical result applies and why the distributions have the form that they
691 do. This is important because it means the result can be applied with greater confidence to periods
692 when inference are only made from proxy data, and in particular, to grand minima like the Maunder
693 minimum.

694 We have developed methods that enable computation of the core distribution of both the ap and
695 (negative) Dst geomagnetic indices for a given annual mean value at a required averaging timescale
696 τ . The algorithms for doing this are detailed in parts (i) and (ii), respectively, of Appendix A. The
697 complications caused by the fact that the Dst index, unlike ap , does not tend to zero when activity is

698 quiet have led to the algorithm for *Dst* being somewhat more involved than that for *ap*, and the
699 distributions are best fitted with a Weibull family of distributions, as opposed to the lognormal
700 family for *ap*.

701 The model distributions for the *ap* index make use of the lognormal form which, as shown in the
702 Supporting Information, gives the best MLE fit of all the distribution forms with two free
703 parameters. The Burr distribution gives slightly better fits according to the absolute goodness-of-fit
704 metrics (least squares and modified Kolmogorov–Smirnov) but the relative metrics that allow for
705 the degrees of freedom (AIC and BIC) show the extra degree of freedom is not justified. (Note that
706 as τ approaches one year and the observed distribution tends towards a Gaussian all the
707 distributions are good fits and differences are minimal). Thus there is no question that the *ap* model
708 employs the best form of distribution (i.e., the lognormal). The model is also relatively
709 straightforward because the *ap* index is unipolar and tends to zero at the quietest activity levels. The
710 largest uncertainty in using the model in even the Maunder minimum relates to the occurrence of
711 CIRs and recurrent disturbances which may influence the model at averaging timescales τ greater
712 than about 25 days.

713 For the *Dst* model these considerations are less straightforward. Firstly, the Weibull, Gamma and
714 log-logistic distributions all perform similarly, and none of them are ideal fits to the observed
715 distribution. Furthermore, the extra degree of freedom of the Burr distribution gives fits that are
716 better by a statistically significant degree. This means the added complexity of using two shape
717 parameters (in addition to the mean $m = 1$) would be worthwhile. However, at this point it is worth
718 remembering that the *Dst* index is, intrinsically, and imperfect metric and hence the additional fit
719 accuracy is unlikely to justify the additional complexity. Hence we propose, in a later paper, to
720 generate a model for the pressure-corrected index *Dst**. Because *Dst** can, like *Dst*, have both
721 positive and negative values and approach similar to that adopted here for *Dst* will be needed.

722 **Acknowledgments and Data**

723 The authors are grateful to the staff of Space Physics Data Facility, NASA/Goddard Space Flight
724 Centre, who prepared and made available the OMNI2 dataset used. The data were downloaded
725 from <http://omniweb.gsfc.nasa.gov/ow.html>. They are also grateful to the staff of
726 GeoForschungsZentrum (GFZ) Potsdam, Adolf-Schmidt-Observatorium für Geomagnetismus,
727 Niemegk, Germany who generate the *ap* data. The *ap* and *aa* data were downloaded from the UK
728 Space Science Data Centre from <https://www.ukssdc.ac.uk/> with updating of recent data from BGS

729 Edinburgh http://www.geomag.bgs.ac.uk/data_service/data/magnetic_indices/apindex.html. The
730 international sunspot data were compiled and made available by WDC-SILSO, Royal Observatory
731 of Belgium, Brussels <http://www.sidc.be/silso/>. The work presented in this paper is supported by
732 STFC consolidated grant number ST/M000885/1, the work of ML and MJO is also supported by
733 the SWIGS NERC Directed Highlight Topic Grant number NE/P016928/1/ and of OA by NERC
734 grant NE/P017274/1. SB is supported by NERC as part of the SCENARIO Doctoral Training
735 Partnership NE/L002566/1.

736 **References**

- 737 Allen, J. H. (1982) Some Commonly Used Magnetic Activity Indices: Their Derivation, Meaning,
738 and Use, in Proceedings of a Workshop on Satellite Drag, March 18-19, 1982, Boulder,
739 Colorado, Ed. J.A.C. Joselyn, pp. 114-134
- 740 Baker, D.N. (2000) The occurrence of operational anomalies in spacecraft and their relationship to
741 space weather. *IEEE Transactions on Plasma Science*, **28**(6), 2007-2016, doi:
742 10.1109/27.902228
- 743 Baker, D. N., X. Li, A. Pulkkinen, C. M. Ngwira, M. L. Mays, A. B. Galvin, and K. D. C. Simunac
744 (2013), A major solar eruptive event in July 2012: Defining extreme space weather scenarios,
745 *Space Weather*, **11**, 585–591, doi:10.1002/swe.20097
- 746 Balan, N., I. S. Batista, S. Tulasiram, and P. K. Rajesh (2016) A new geomagnetic storm parameter
747 for the severity of space weather, *Geosci. Lett.*, **3**, 3, doi:10.1186/s40562-016-0036-5.
- 748 Balch, C. C. (2008) Updated verification of the Space Weather Prediction Center's solar energetic
749 particle prediction model, *Space Weather*, **6**, S01001, doi:10.1029/2007SW000337
- 750 Barnard, L.A., M. Lockwood, M.A. Hapgood, M.J. Owens, C.J. Davis, and F. Steinhilber (2011)
751 Predicting Space Climate Change, *Geophys. Res. Lett.*, **38**, L16103, doi:
752 10.1029/2011GL048489
- 753 Barnard, L. A., C. A. de Koning, C. J. Scott, M. J. Owens, J. Wilkinson, and J. A. Davies (2017),
754 Testing the current paradigm for space weather prediction with heliospheric imagers, *Space*
755 *Weather*, **15**, 782–803, doi: 10.1002/2017SW001609.
- 756 Beirlant, J., Y. Goegebeur, J. Segers, and J. Teugels (2004), *Statistics of Extremes*, John Wiley,
757 Chichester, U.K., doi: 10.1002/0470012382
- 758 Borovsky, J.E. (2017) Time-integral correlations of multiple variables with the relativistic electron
759 flux at geosynchronous orbit: The strong roles of substorm injected electrons and the ion
760 plasma sheet, *J. Geophys. Res.*, **122**, doi:10.1002/2017JA024476.
- 761 Boteler, D.H. (2000) Geomagnetic effects on the pipe-to-soil potentials of a continental pipeline, In
762 *Adv. Space Res.*, **26** (1), 15-20, doi: 10.1016/S0273-1177(99)01020-0
- 763 Chapman, S.C., N. W. Watkins, and E. Tindale, (2018) Reproducible aspects of the climate of
764 space weather over the last five solar cycles, *Space Weather*, **16** (8), 1128–1142. doi:
765 10.1029/2018SW001884
- 766 Chen, M. W., L. R. Lyons, and M. Schulz (2000) Stormtime ring-current formation: A comparison
767 between single-and double-dip model storms with similar transport characteristics, *J.*
768 *Geophys. Res.*, **105** (A12), 27755–27765, doi:10.1029/1999JA000440.

- 769 Cliver E.W. and W.F. Dietrich (2013), The 1859 space weather event revisited: limits of extreme
770 activity, *J. Space Weather Space Clim.*, **3**, 2013, A31, pp. 1-15, doi: 10.1051/swsc/2013053
- 771 Cliver, E.W. and L. Svalgaard (2004) The 1859 solar–terrestrial disturbance and the current limits
772 of extreme space weather activity, *Solar Physics*, **224** (1-2), 407-422, doi: 10.1007/s11207-
773 005-4980-z
- 774 Cole, D.G. (2003) Space weather: its effects and predictability, *Space Science Reviews*, 107 (1/2),
775 295-302, doi: 10.1023/A:1025500513499
- 776 Coles, S. (2004) An Introduction to Statistical Modelling of Extreme Values, Springer, London
- 777 Consolini, G., P. De Michelis, and R. Tozzi (2008), On the Earth’s magnetospheric dynamics:
778 Nonequilibrium evolution and the fluctuation theorem, *J. Geophys. Res.*, **113**, A08222,
779 doi:10.1029/2008JA013074.
- 780 Daglis, I. A. (1997) The Role of Magnetosphere-Ionosphere Coupling in Magnetic Storm
781 Dynamics, in *Magnetic Storms* (eds B. T. Tsurutani, W. D. Gonzalez, Y. Kamide and J. K.
782 Arballo), American Geophysical Union, Washington, D. C.. doi: 10.1029/GM098p0107
- 783 Dmitriev, A. V., A.V. Suvorova, and I.S. Veselovsky (2009) Statistical Characteristics of the
784 Heliospheric Plasma and Magnetic Field at the Earth's Orbit during Four Solar Cycles 20-23,
785 in Handbook on solar wind; in *Handbook on Solar Wind: Effects, Dynamics and Interactions*,
786 Ed. Hans E. Johannson, NOVA Science Publishers, Inc., New York, p. 81-144. eprint
787 arXiv:1301.2929
- 788 Doornbos, E., and H. Klinkrad (2006) Modelling of space weather effects on satellite drag, *Adv.*
789 *Space Res.*, **37** (6), 1229-1239, doi: 10.1016/j.asr.2005.04.097
- 790 Echer, E., W. D. Gonzalez, and B. T. Tsurutani (2008) Interplanetary conditions leading to
791 superintense geomagnetic storms ($Dst \leq -250$ nT) during solar cycle 23, *Geophys. Res. Lett.*,
792 **35**, L06S03, doi:10.1029/2007GL031755.
- 793 Farrugia, C.J., B. Harris, M. Leitner, C. Möstl, A.B. Galvin, K.D.C. Simunac, R.B. Torbert, M.B.
794 Temmer, A.M. Veronig, N.V. Erkaev, A. Szabo, K.W. Ogilvie, J.G. Luhmann, and V.A.
795 Osherovich (2012) Deep Solar Activity Minimum 2007 – 2009: Solar Wind Properties and
796 Major Effects on the Terrestrial Magnetosphere, *Solar Phys*, **281**, 461–489, 2012, doi:
797 10.1007/s11207-012-0119-1
- 798 Fischer, H. (2011) A History of the Central Limit Theorem, from Classical to Modern Probability
799 Theory, book in series “*Sources and Studies in the History of Mathematics and Physical*
800 *Sciences*”, Springer, New York, doi:10.1007/978-0-387-87857-7
- 801 Fleetwood, D.M. P.S. Winokur, P.E. Dodd (2000) An overview of radiation effects on electronics
802 in the space telecommunications environment, *Microelectronics Reliability*, 40 (1), 17-26,
803 doi: 10.1016/S0026-2714(99)00225-5.

- 804 Gaunt, C. T. (2016), Why Space Weather Is Relevant to Electrical Power Systems, *Space Weather*,
805 **14**, 2–9, doi:10.1002/2015SW001306.
- 806 Gummow, R.A. (2002) GIC effects on pipeline corrosion and corrosion control systems, *J. Atmos.*
807 *and Sol.-Terr. Phys.*, **64** (16), 1755-1764, doi: 10.1016/S1364-6826(02)00125-6.
- 808 Hamilton, D. C., G. Gloeckler, F. M. Ipavich, W. Stüdemann, B. Wilken, and G. Kremser (1988)
809 Ring current development during the great geomagnetic storm of February 1986, *J. Geophys.*
810 *Res.*, **93** (A12), 14343–14355, doi: 10.1029/JA093iA12p14343.
- 811 Hapgood, M.A., G. Bowe, M. Lockwood, D.M. Willis, and Y. Tulunay (1991) Variability of the
812 interplanetary magnetic field at 1 A.U. over 24 years: 1963 – 1986, *Planet. Space Sci.*, **39**,
813 411-423, doi: 10.1016/0032-0633(91)90003-S
- 814 Hamill, T. M. and Juras, J. (2006) Measuring forecast skill: is it real skill or is it the varying
815 climatology?, *Q.J.R. Meteorol. Soc.*, **132**, 2905–2923, doi: 10.1256/qj.06.25
- 816 Henley, E. M., and E.C.D. Pope (2017) Cost-loss analysis of ensemble solar wind forecasting:
817 Space weather use of terrestrial weather tools, *Space Weather*, **15**, doi:
818 10.1002/2017SW001758
- 819 Heyde, C. (2006) Central Limit Theorem, in *Encyclopedia of Actuarial Science*, 1, John Wiley and
820 Sons, doi: 10.1002/9780470012505.tac019
- 821 Ingham, M., & Rodger, C. J. (2018). Telluric field variations as drivers of variations in cathodic
822 protection potential on a natural gas pipeline in New Zealand. *Space Weather*, **16**, 1396-1409.
823 <https://doi.org/10.1029/2018SW001985>.
- 824 Kappenman, J. G. (2005), An overview of the impulsive geomagnetic field disturbances and power
825 grid impacts associated with the violent Sun-Earth connection events of 29–31 October 2003
826 and a comparative evaluation with other contemporary storms, *Space Weather*, **3**, S08C01,
827 doi: 10.1029/2004SW000128.
- 828 Kappenman, J. G. and Radasky, W. A. (2005), Too Important to Fail, *Space Weather*, **3**:
829 doi:10.1029/2005SW000152
- 830 Kauristie, K., A. Morschhauser, N. Olsen, C.C. Finlay, R.L. McPherron, J.W. Gjerloev, and H.J.
831 Opgenoorth (2017) On the Usage of Geomagnetic Indices for Data Selection in Internal Field
832 Modelling, *Space Sci. Rev.*, **206** (1-4), 61-90, doi: 10.1007/s11214-016-0301-0
- 833 Knipp, D. J. (2016), Advances in Space Weather Ensemble Forecasting, *Space Weather*, **14**, 52–53,
834 doi: 10.1002/2016SW001366.
- 835 Koons, H. C. (2001), Statistical analysis of extreme values in space science, *J. Geophys. Res.*, **106**,
836 10,915–10,921, doi: 10.1029/2000JA000234

- 837 Kotz, S. and S. Nadarajah (2000) Extreme Value Distributions: Theory and Applications, World
838 Scientific, doi: org/10.1142/p191
- 839 Kozyra, J. U., J. E. Borovsky, M. W. Chen, M.-C. Fok, and V. K. Jordanova (1998) Plasma sheet
840 preconditioning, enhanced convection and ring current development, in *Substorms-4*, edited
841 by S. Kokubun, and Y. Kamide, pp. 755–760, Terra Sci., Tokyo, doi: 10.1007/978-94-011-
842 4798-9_158
- 843 Kozyra, J. U., M. W. Liemohn, C. R. Clauer, A. J. Ridley, M. F. Thomsen, J. E. Borovsky, J. L.
844 Roeder, V. K. Jordanova, and W. D. Gonzalez (2002) Multistep Dst development and ring
845 current composition changes during the 4–6 June 1991 magnetic storm, *J. Geophys. Res.*, **107**
846 (A8), 1224, doi: 10.1029/2001JA000023.
- 847 Lang, M., P. Browne, P.J. van Leeuwen and M.J. Owens (2017) Data Assimilation in the Solar
848 Wind: Challenges and First Results, *Space Weather* **15**, 1490–1510, doi:
849 10.1002/2017SW001681
- 850 Lefèvre, L., S. Vennerstrøm, M. Dumbović, B. Vršnak, D. Sudar, R. Arlt, F. Clette, N. Crosby
851 (2016) Detailed Analysis of Solar Data Related to Historical Extreme Geomagnetic Storms:
852 1868 – 2010, *Solar Phys*, **291**, 1483–1531, doi: 10.1007/s11207-016-0892-3
- 853 Lockwood, M. (2003) Twenty-three cycles of changing open solar flux, *J. Geophys. Res.*, **108** (A3),
854 1128, doi: 10.1029/2002JA009431.
- 855 Lockwood, M. (2013) Reconstruction and Prediction of Variations in the Open Solar Magnetic
856 Flux and Interplanetary Conditions, *Living Reviews in Solar Physics*, **10**, 4, doi:
857 10.12942/lrsp-2013-4
- 858 Lockwood, M. and M.J. Owens (2014a) Implications of the recent low solar minimum for the solar
859 wind during the Maunder minimum, *Astrophys. J. Lett.*, **781**, L7, doi:10.1088/2041-
860 8205/781/1/L7
- 861 Lockwood, M. and M.J. Owens (2014b) Centennial variations in sunspot number, open solar flux
862 and streamer belt width: 3. Modelling, *J. Geophys. Res. Space Physics*, **119** (7), 5193-5209,
863 doi: 10.1002/2014JA019973
- 864 Lockwood, M., and M.N. Wild (1993) On the quasi-periodic nature of magnetopause flux transfer
865 events, *J. Geophys. Res.*, **98**, 5935-5940, doi: 10.1029/92JA02375.
- 866 Lockwood, M., R. Stamper and M.N. Wild (1999) A doubling of the sun's coronal magnetic field
867 during the last 100 years, *Nature*, **399**, 437-439, doi: 10.1038/20867
- 868 Lockwood, M., A.P. Rouillard, and I.D. Finch (2009) The rise and fall of open solar flux during the
869 current grand solar maximum, *Ap. J.*, **700** (2), 937-944, doi: 10.1088/0004-637X/700/2/937,
870 2009

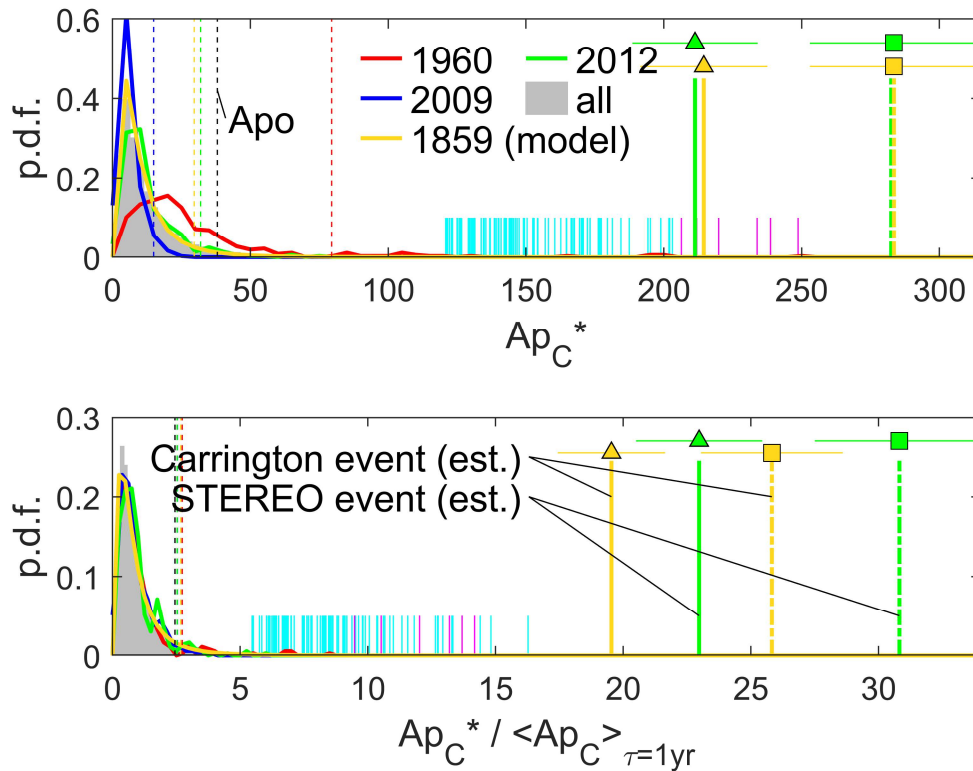
- 871 Lockwood, M., H. Nevanlinna, L. Barnard, M.J. Owens, R.G. Harrison, A.P. Rouillard, and C.J.
872 Scott (2014) Reconstruction of Geomagnetic Activity and Near-Earth Interplanetary
873 Conditions over the Past 167 Years: 4. Near-Earth Solar Wind Speed, IMF, and Open Solar
874 Flux, *Annales. Geophys.*, **32**, 383-399, doi: 10.5194/angeo-32-383-2014
- 875 Lockwood, M., M.J. Owens, L.A. Barnard S. Bentley, C.J. Scott, and C.E. Watt (2016) On the
876 Origins and Timescales of Geoeffective IMF, *Space Weather*, **14**, 406–432, doi:
877 10.1002/2016SW001375
- 878 Lockwood, M., M.J. Owens, L.A. Barnard, C.J. Scott, and C.E. Watt (2017a) Space Climate and
879 Space Weather over the past 400 years: 1. The Power input to the Magnetosphere, *J. Space
880 Weather Space Clim.*, **7**, A25, doi: 10.1051/swsc/2017019
- 881 Lockwood, M., M.J. Owens, L.A. Barnard, C.J. Scott, C.E. Watt and S. Bentley (2018a) Space
882 Climate and Space Weather over the past 400 years: 2. Proxy indicators of geomagnetic storm
883 and substorm occurrence, *J. Space Weather Space Clim.*, in press, doi: 10.1051/swsc/2017048
- 884 Lockwood, M., S. Bentley, M.J. Owens, L.A. Barnard, C.J. Scott, C.E. Watt and O. Allanson
885 (2018b) The development of a space climatology: 1. Solar-wind magnetosphere coupling as a
886 function of timescale and the effect of data gaps, *Space Weather*, in press
- 887 Lockwood, M., S. Bentley, M.J. Owens, L.A. Barnard, C.J. Scott, C.E. Watt and O. Allanson
888 (2018c) The development of a space climatology: 2. the variation of space weather
889 parameters with timescale, *Space Weather*, in press
- 890 Lockwood, M., A. Chambodut, L.A. Barnard, M.J. Owens, E. Clarke, and V. Mendel (2018d) A
891 homogeneous aa index: 1. Secular variation, *J. Space Weather Space Clim.*, in press,
892 10.1051/swsc/2018038
- 893 Lockwood, M., I.D. Finch, A. Chambodut, L.A. Barnard, M.J. Owens, and E. Clarke (2018e) A
894 homogeneous aa index: 2. hemispheric asymmetries and the equinoctial variation, *J. Space
895 Weather Space Clim.*, in press. 10.1051/swsc/2018044
- 896 Lotz, S.I. and D.W. Danskin (2017) Extreme value analysis of induced geoelectric field in South
897 Africa, *Space Weather*, **15**, doi:10.1002/2017SW001662.
- 898 Love, J. J. (2012), Credible occurrence probabilities for extreme geophysical events: Earthquakes,
899 volcanic eruptions, magnetic storms, *Geophys. Res. Lett.*, **39**, L10301,
900 doi:10.1029/2012GL051431.
- 901 Love, J. J., Rigler, E. J., Pulkkinen, A., & Riley, P. (2015) On the lognormality of historical
902 magnetic storm intensity statistics: Implications for extreme-event probabilities. *Geophysical
903 Research Letters*, **42**, 6544–6553, doi: 10.1002/2015gl064842
- 904 Matthes, K., B. Funke, M.E.Andersson, L. Barnard, J. Beer, P. Charbonneau, M.A. Clilverd, T.
905 Dudok de Wit, M. Haberreiter, A. Hendry, C.H. Jackman, M. Kretschmar, T. Kruschke, M.

- 906 Kunze, U. Langematz, D.R. Marsh, A. Maycock, S. Misios, C.J. Rodger, A.A. Scaife, A.
 907 Seppälä, M. Shangguan, M. Sinnhuber, K. Tourpali, I. Usoskin, M. van de Kamp, P.T.
 908 Verronen, and S. Versick (2017) Solar Forcing for CMIP6 *Geosci. Model Dev.*, **10**, 2247-
 909 2302, doi: 10.5194/gmd-10-2247-2017
- 910 Mayaud, P.-N. (1972) The *aa* indices: A 100-year series characterizing the magnetic activity, *J.*
 911 *Geophys. Res.*, **77**, 6870–6874, doi: 10.1029/JA077i034p06870
- 912 Mayaud, P.-N. (1980) Derivation, Meaning and Use of Geomagnetic Indices, Geophysical
 913 Monograph, **22**, American Geophysical Union, Washington, DC, doi: 10.1029/GM022
- 914 Menvielle, M., and A. Berthelier (1991) The K-derived planetary indices: Description and
 915 availability, *Rev. Geophys.*, **29** (3), 415–432, doi: 10.1029/91RG00994.
- 916 Mourenas D., A.V Artemyev, and X.-J. Zhang (2018), Statistics of extreme time integrated
 917 geomagnetic activity, *Geophys. Res. Lett.*, **44**, doi:10.1002/2017GL076828.
- 918 Nevanlinna, H. (2006) A study on the great geomagnetic storm of 1859: Comparisons with other
 919 storms in the 19th century, *Adv. Space Res.*, **38** (2), 180–187, doi: 10.1016/j.asr.2005.07.076.
- 920 Ngwira, C.M., A. Pulkkinen, M. Leila Mays, M.M. Kuznetsova, A.B. Galvin, K. Simunac, D.N.
 921 Baker, X. Li, Y. Zheng, and A. Gloer (2013), Simulation of the 23 July 2012 extreme space
 922 weather event: What if this extremely rare CME was Earth directed?, *Space Weather*, **11**,
 923 671–679, doi:10.1002/2013SW000990.
- 924 Ngwira, C.M., A. Pulkkinen, M.M. Kuznetsova, and A. Gloer (2014), Modeling extreme
 925 “Carrington-type” space weather events using three-dimensional global MHD simulations, *J.*
 926 *Geophys. Res. Space Physics*, **119**, 4456–4474, doi: 10.1002/2013JA019661.
- 927 O'Brien, T. P., and R. L. McPherron (2000) An empirical phase space analysis of ring current
 928 dynamics: Solar wind control of injection and decay, *J. Geophys. Res.*, **105** (A4), 7707–7719,
 929 doi: 10.1029/1998JA000437.
- 930 O'Brien, T. P., J. F. Fennell, J. L. Roeder, and G. D. Reeves (2007), Extreme electron fluxes in the
 931 outer zone, *Space Weather*, **5**, S01001, doi:10.1029/2006SW000240
- 932 Owens, M. J., and P. Riley (2017) Probabilistic solar wind forecasting using large ensembles of
 933 near-Sun conditions with a simple one-dimensional “upwind” scheme. *Space Weather*, **15**,
 934 doi: 10.1002/2017SW001679
- 935 Owens, M.J. M. Lockwood and I. Usoskin (2012) Heliospheric modulation of galactic cosmic rays
 936 during grand solar minima: Past and future variations, *Geophys. Res. Lett.*, **39**, L19102, 2012.
 937 doi:10.1029/2012GL053151
- 938 Owens, M.J., E. Cliver, K. McCracken, J. Beer, L.A. Barnard, M. Lockwood, A.P. Rouillard, D.
 939 Passos, P. Riley, I.G. Usoskin, Y.-M. Wang (2016a) Near-Earth Heliospheric Magnetic Field

- 940 Intensity since 1800. Part 1: Sunspot and Geomagnetic Reconstructions, *J. Geophys. Res.*,
941 **121** (7), 6048-6063, doi: 10.1002/2016JA022529
- 942 Owens, M.J., E. Cliver, K. McCracken, J. Beer, L.A. Barnard, M. Lockwood, A.P. Rouillard, D.
943 Passos, P. Riley, I.G. Usoskin, Y.-M. Wang (2016b) Near-Earth Heliospheric Magnetic Field
944 Intensity since 1800. Part 2: Cosmogenic Radionuclide Reconstructions, *J. Geophys. Res.*,
945 **121** (7), 6064-6074, doi: 10.1002/2016JA022550
- 946 Owens, M.J., M. Lockwood, P. Riley (2017) Global solar wind variations over the last four
947 centuries, *Scientific Reports.*, **7**, Article number 41548, doi:10.1038/srep41548
- 948 Pirjola, R. (2005) Effects of space weather on high-latitude ground systems, *Adv. Space Res.*, **36**,
949 Issue 12, 2005, Pages 2231-2240, ISSN 0273-1177, doi: 10.1016/j.asr.2003.04.074.
- 950 Pirjola, R., K. Kauristie, H. Lappalainen, A. Viljanen, and A. Pulkkinen (2005), Space weather risk,
951 *Space Weather*, **3**, S02A02, doi:10.1029/2004SW000112
- 952 Pizzo, V.J., C. de Koning, M. Cash, G. Millward, D.A. Biesecker, L. Puga, M. Codrescu, and D.
953 Odstrcil (2015) Theoretical basis for operational ensemble forecasting of coronal mass
954 ejections, *Space Weather*, **13**, 676–697, doi:10.1002/2015SW001221.
- 955 Pulkkinen, A., R. Pirjola, D. Boteler, A. Viljanen, I. Yegorov (2001) Modelling of space weather
956 effects on pipelines, *J. Applied Geophysics*, **48** (4), 233-256, doi: 10.1016/S0926-
957 9851(01)00109-4.
- 958 Riley, P. (2012), On the probability of occurrence of extreme space weather events, *Space Weather*,
959 **10**, S02012, doi:10.1029/2011SW000734.
- 960 Riley, P., and J. J. Love (2017) Extreme geomagnetic storms: Probabilistic forecasts and their
961 uncertainties, *Space Weather*, **15**, 53–64, 2017, doi: 10.1002/2016SW001470
- 962 Schunk, R. W., et al. (2014) Ensemble Modeling with Data Assimilation Models: A New Strategy
963 for Space Weather Specifications, Forecasts, and Science, *Space Weather*, **12**, 123–126,
964 doi:10.1002/2014SW001050.
- 965 Shea, M.A. and D.F. Smart (2006) Compendium of the eight articles on the “Carrington Event”
966 attributed to or written by Elias Loomis in the American Journal of Science, 1859-1861, *Adv.*
967 *Space Res.*, **38** (2), 313-385, doi: 10.1016/j.asr.2006.07.005.
- 968 Silbergleit, V. M. (1996), On the occurrence of geomagnetic storms with sudden commencements,
969 *J. Geomagn. Geoelectr.*, **48**, 1011–1016, doi:10.5636/jgg.48.1011
- 970 Silbergleit, V. M. (1999), Forecast of the most geomagnetically disturbed days, *Earth Planets*
971 *Space*, **51**, 19–22, doi: 10.1186/bf03352205

- 972 Siscoe, G. L. (1976), On the statistics of the largest geomagnetic storms per solar cycle, *J.*
 973 *Geophys. Res.*, **81**(25), 4782–4784, doi: 10.1029/JA081i025p04782
- 974 Siscoe, G., and S.C. Solomon (2006) Aspects of data assimilation peculiar to space weather
 975 forecasting, *Space Weather*, **4**, S04002, doi:10.1029/2005SW000205.
- 976 Stern, D. (2002) A millennium of geomagnetism, *Rev. Geophys.*, **40** (3), 1007, doi:
 977 10.1029/2000RG000097
- 978 Svalgaard, L., and E. W. Cliver (2010) Heliospheric magnetic field 1835–2009, *J. Geophys. Res.*,
 979 **115**, A09111, 2010, doi: 10.1029/2009JA015069
- 980 Thomson, A. W. P., E. B. Dawson, and S. J. Reay (2011), Quantifying extreme behavior in
 981 geomagnetic activity, *Space Weather*, **9**, S10001, doi:10.1029/2011SW000696.
- 982 Tindale, E., Chapman, S. C., Moloney, N. R., & Watkins, N. (2018). The dependence of solar wind
 983 burst size on burst duration and its invariance across solar cycles 23 and 24. *Journal of*
 984 *Geophysical Research: Space Physics*, **16** (8), 1128-1142, doi:10.1029/2018JA025740
- 985 Tsubouchi, K., and Y. Omura (2007), Long-term occurrence probabilities of intense geomagnetic
 986 storm events, *Space Weather*, **5**, S12003, doi:10.1029/2007SW000329.
- 987 Tsurutani, B.T., Y. Kamide, J.K. Arballo, W.D. Gonzalez, R.P. Lepping (1999) Interplanetary
 988 causes of great and superintense magnetic storms, *Physics and Chemistry of the Earth, Part*
 989 *C: Solar, Terrestrial & Planetary Science*, **24** (1-3), 101-105, doi: 10.1016/S1464-
 990 1917(98)00015-4.
- 991 Turner, N. E., D. N. Baker, T. I. Pulkkinen, and R. L. McPherron (2000) Evaluation of the tail
 992 current contribution to Dst, *J. Geophys. Res.*, **105** (A3), 5431–5439,
 993 doi:10.1029/1999JA000248.
- 994 Usoskin, I.G., R. Arlt, E. Asvestari, E. Hawkins, M. Käpylä, G.A. Kovaltsov, N. Krivova, M.
 995 Lockwood, K. Mursula, J. O'Reilly, M. Owens, C. J. Scott, D. D. Sokoloff, S. K. Solanki, W.
 996 Soon, and J. M. Vaquero (2015) The Maunder minimum (1645-1715) was indeed a Grand
 997 minimum: A reassessment of multiple datasets, *Astron. and Astrophys.*, **581**, A95, doi:
 998 10.1051/0004-6361/201526652
- 999 Vaselovsky, I.S., A.V. Dmitriev, and A.V. Suvorova (2010) Lognormal, Normal and Other
 1000 Distributions Produced by Algebraic Operations in *The Solar Wind*, AIP Conference
 1001 Proceedings 1216, 152 -155, doi: 10.1063/1.3395824
- 1002 Vasyliunas, V. M., J. R. Kan, G. L. Siscoe, and S.-I. Akasofu (1982) Scaling relations governing
 1003 magnetospheric energy transfer, *Planet. Space Sci.*, **30**, 359–365, doi: 10.1016/0032-
 1004 0633(82)90041-1

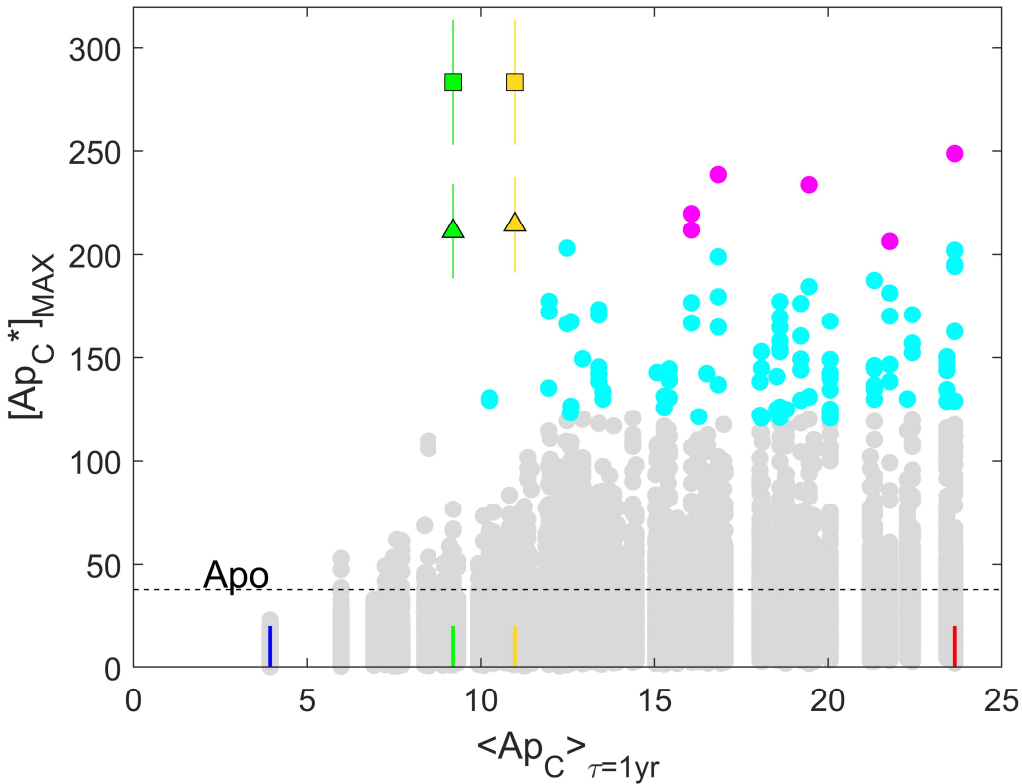
- 1005 Viljanen, A., A. Pulkkinen, R. Pirjola, K. Pajunpää, P. Posio, and A. Koistinen (2006), Recordings
1006 of geomagnetically induced currents and a nowcasting service of the Finnish natural gas
1007 pipeline system, *Space Weather*, **4**, S10004, doi:10.1029/2006SW000234
- 1008 Vörös Z., M. Leitner, Y. Narita, G. Consolini, P. Kovács, A. Tóth, and J. Lichtenberger (2015)
1009 Probability density functions for the variable solar wind near the solar cycle minimum, *J.*
1010 *Geophys. Res. Space Physics*, **120**, 6152–6166, doi:10.1002/2015JA021257
- 1011 Weigel, R.S. and D.N. Baker (2003) Probability distribution invariance of 1-minute auroral-zone
1012 geomagnetic field fluctuations, *Geophys. Res. Lett.*, **30** (23), 2193,
1013 doi:10.1029/2003GL018470
- 1014 Wilkes, D.S. (1995) Statistical methods in the atmospheric sciences, second edition, *International*
1015 *Geophysics Series*, Vol 59, Academic Press, 464pp. ISBN-10: 0127519653. ISBN-13: 978-
1016 0127519654.
- 1017 Woody, M.S., J.H. Lewis, M.J. Greenberg, Y.E. Goldman, E.M. Ostap (2016) MEMLET: An
1018 Easy-to-Use Tool for Data Fitting and Model Comparison Using Maximum-Likelihood
1019 Estimation, *Biophysical J.*, **111** (2), 273 to 282, doi: 10.1016/j.bpj.2016.06.019
- 1020 Xie, H., N. Gopalswamy, P. K. Manoharan, A. Lara, S. Yashiro, and S. T. Lepri (2006) Long-lived
1021 geomagnetic storms and coronal mass ejections, *J. Geophys. Res.*, **111**, A01103, doi:
1022 10.1029/2005JA011287.
- 1023 Xiang, N.B. and Z. N. Qu (2018) Evolutionary Characteristics of the Interplanetary Magnetic Field
1024 Intensity, *Ap. J.*, **156** (4), 152. doi: 10.3847/1538-3881/aadb91
- 1025



1026

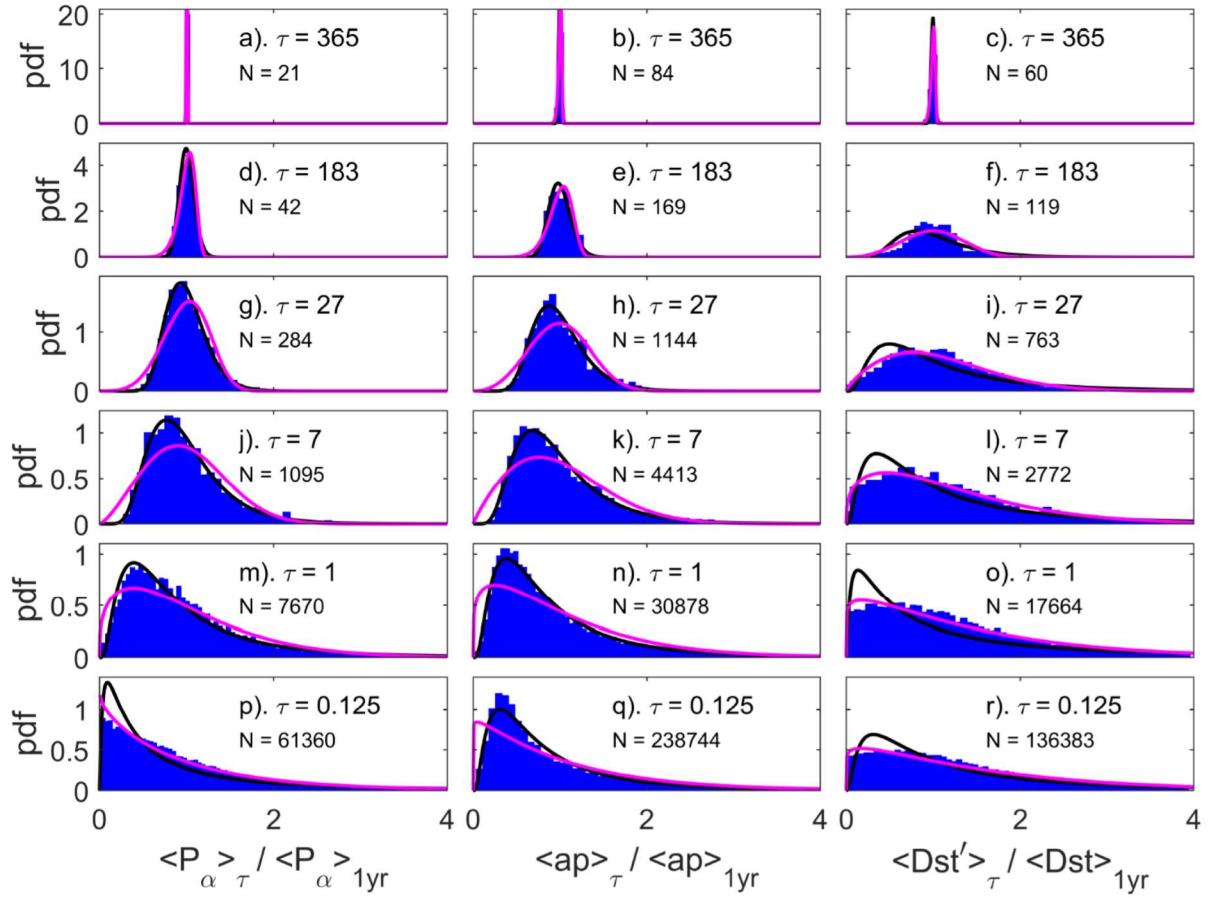
1027 **Figure 1.** Distributions of ap_C , the ap index corrected for the annual variation in its response
 1028 function, (see Appendix B). Annual distributions of (top) 8-point running (boxcar) means of the
 1029 three-hourly ap_C values, Ap_C^* , and (bottom) of those means as a ratio of the annual mean value for
 1030 the calendar year in question, $Ap_C^*/\langle ap_C \rangle_{\tau=1\text{yr}}$, for: (red) 1960; (blue) 2009; (green) 2012; and
 1031 (orange) modelled for 1859. The gray histograms in the background are the distributions for all
 1032 248368 Ap_C^* values available from the interval 1932-2016. The vertical orange lines mark the
 1033 estimated value for the peak of the 1859 Carrington event: the solid orange line is “estimate 1”,
 1034 $[Ap_C^*]_{\text{MAX}}$ which makes allowance for the time-of-year response of the ap index (also marked by
 1035 an orange triangle), the dot-dash orange line is $[Ap^*]_{\text{MAX}}$ which does not make this correction
 1036 (“estimate 2”, also marked by an orange square). The uncertainty bars arise only from the
 1037 conversion of Aa^* to Ap^* and do not include the uncertainty in the Aa^* estimate. The distributions
 1038 for 2012 are shown because in that year an event, that it is estimated would have caused an extreme
 1039 event almost as large as the Carrington event, passed over the STEREO A craft but missed the
 1040 Earth: the vertical green lines show the estimated maximum for that event, had it hit Earth: the solid

1041 green line and green triangle is for the $[Ap_C^*]_{MAX}$ (estimate 1) value and the dot-dash green line and
1042 green square are for the $[Ap^*]_{MAX}$ (estimate 2) value. The vertical coloured dashed lines give the
1043 95-percentiles of the annual distributions, using the same color scheme and the vertical black
1044 dashed lines are the equivalent for Apo , the 95th percentile of all Ap_C^* values. The short vertical
1045 cyan lines show the top 100 (0.32%) of the maximum Ap_C^* values in a calendar day, $[Ap_C^*]_{MAX}$,
1046 and the short vertical mauve lines $[Ap_C^*]_{MAX}$ values are the 6 days in the top 0.02%. The top 100
1047 events, with further details, are listed in Part 3 of the Supporting Information file.



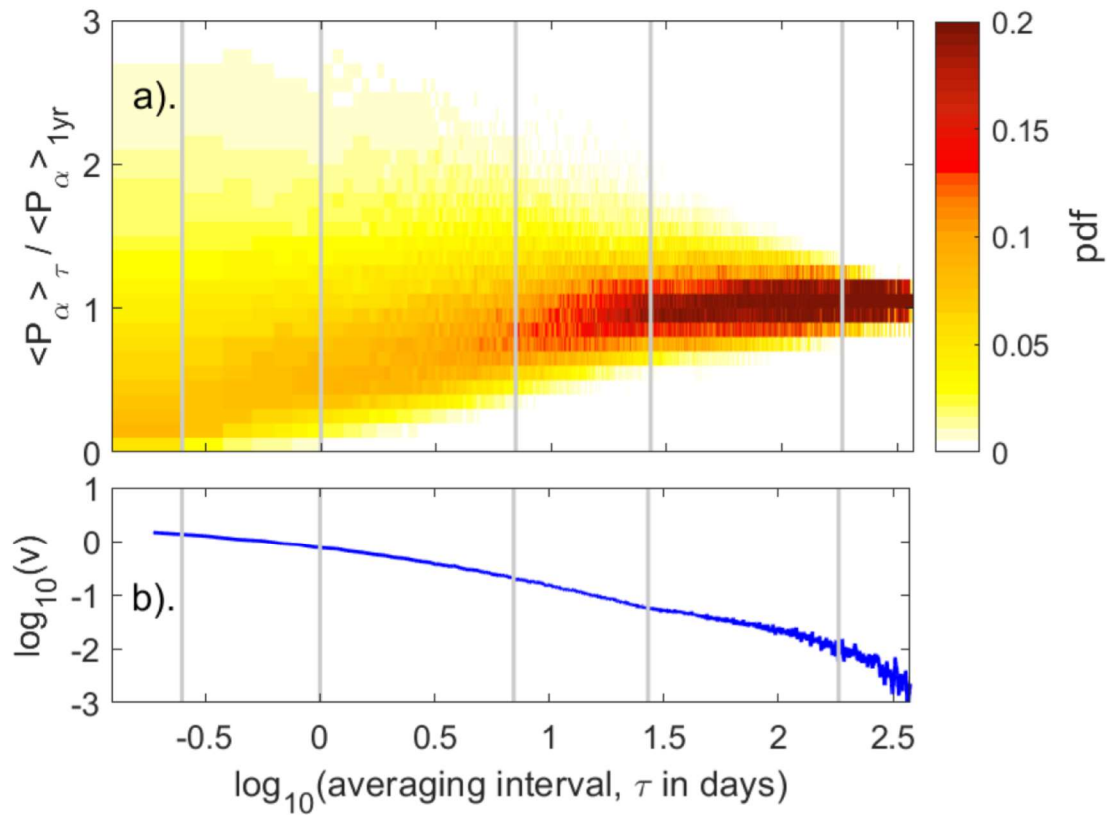
1048

1049 **Figure 2.** The largest Ap_C^* values in a calendar day, $[Ap_C^*]_{MAX}$, as a function of the annual mean
 1050 for the calendar year of that day $\langle ap_C \rangle_{\tau=1yr}$ for 1932-2016 (inclusive). The grey points make up
 1051 99.68% of the available 31047 daily $[Ap_C^*]_{MAX}$ samples, the cyan points being in the top 100 days
 1052 in terms of their $[Ap_C^*]_{MAX}$ value (also shown by the short vertical cyan lines in Figure 1) and the
 1053 mauve points the 6 days in the top 0.02% (shown by the short vertical mauve lines in Figure 1).
 1054 The top 100 days are listed in the Supporting Information file. The orange and green triangles show
 1055 the estimated $[Ap_C^*]_{MAX}$ values for the Carrington and STEREO-A events (in 1859 and 2012,
 1056 respectively, see text for details) and the orange and green squares show the corresponding
 1057 uncorrected $[Ap^*]_{MAX}$ values. The uncertainty bars arise only from the conversion of Aa^* to Ap^*
 1058 and do not include any uncertainty in the Aa^* estimate. The horizontal dashed line is Apo , the 95th
 1059 percentile of all Ap_C^* values. The colored tickmarks along the x axis mark the annual means of the
 1060 four annual distributions shown in Figure 1 (from left to right 2009, 2012, 1859 and 1960), using
 1061 the same color scheme

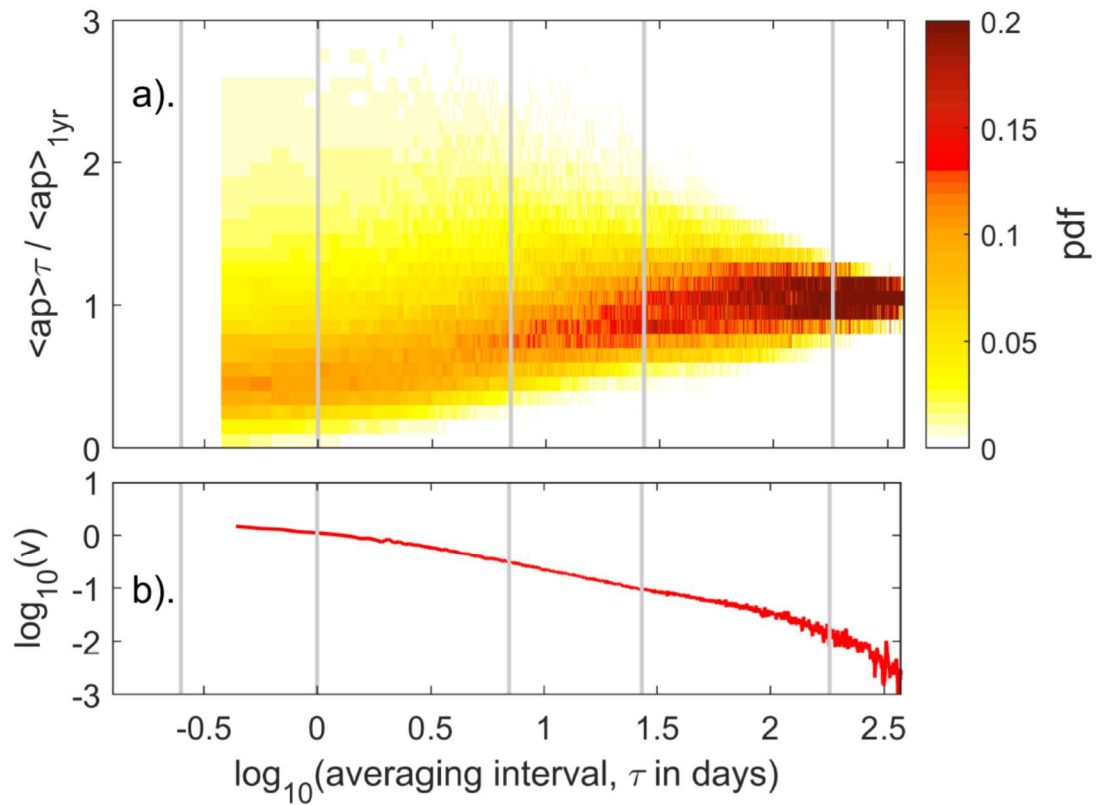


1062
 1063 **Figure 3.** Distributions of (left hand panels) normalized power input into the magnetosphere,
 1064 $\langle P_\alpha \rangle_\tau / \langle P_\alpha \rangle_{1\text{yr}}$; (central panels) normalized geomagnetic ap index, $\langle ap \rangle_\tau / \langle ap \rangle_{1\text{yr}}$; and (right hand
 1065 panels) normalized negative geomagnetic Dst index, $\langle Dst' \rangle_\tau / \langle Dst \rangle_{1\text{yr}}$. The coupling function of
 1066 $\alpha = 0.44$, shown in Paper 1 to apply at all τ , is used to generate P_α . The distributions are of the
 1067 means taken over intervals τ long, divided by the annual mean of all samples in that year. The blue
 1068 histograms are the observed distributions, with samples binned into 150 contiguous bins centered
 1069 on $k \cdot x_{98} / 100$ where k is varied between 0.5 and 149.5 in steps of 1 and x_{98} is the 98th percentile of
 1070 the c.d.f. and the numbers of samples n are then normalized such that $(x_{98} / 100) \sum n$ is unity. The
 1071 black lines shows the best-fit lognormal distributions and the mauve lines are the best-fit Weibull
 1072 distributions (with mean value $m = 1$ in the cases of P_α and ap and $m = Rm(\tau)$ for Dst'). Fits are
 1073 made using Maximum Likelihood Estimation (see the Supporting Information file). The total
 1074 number of available samples, N , is given in each panel. (a), (b) and (c) are for $\tau = 1\text{yr}$; (d), (e) and
 1075 (f) for $\tau = 0.5\text{yr}$; (g), (h) and (i) for $\tau = 27\text{dy}$; (j), (k) and (l) for $\tau = 7\text{ day}$; (m), (n) and (o) for $\tau = 1$

1076 day; and (p), (q) and (r) for $\tau = 3\text{hr}$. The P_α data are from 1996-2016 (inclusive), the ap data for
1077 1932-2016 (inclusive) and the Dst' data are for 1957-2016 (inclusive). $\langle Dst \rangle_\tau \geq 0$ samples are
1078 omitted giving Dst' (so because all $\langle Dst \rangle_{1\text{yr}}$ values are negative, these give $\langle Dst' \rangle_\tau / \langle Dst \rangle_{1\text{yr}} \geq$
1079 0) in histograms and distribution fits: as a result N for Dst' is 100%, 99.17%, 94.08%, 88.42%,
1080 80.60%, and 78.48% of all Dst samples for τ of, respectively, 1yr. (panel c), 0.5yr. (panel f), 27days
1081 (panel i), 7 days (panel l), 1 day (panel o), and 3hr. (panel r). The best-fit distribution parameters,
1082 goodness-of-fit metrics and c.d.f and p.d.f plots are given in the Supporting Information file for
1083 these two fitted distributions and 5 others.



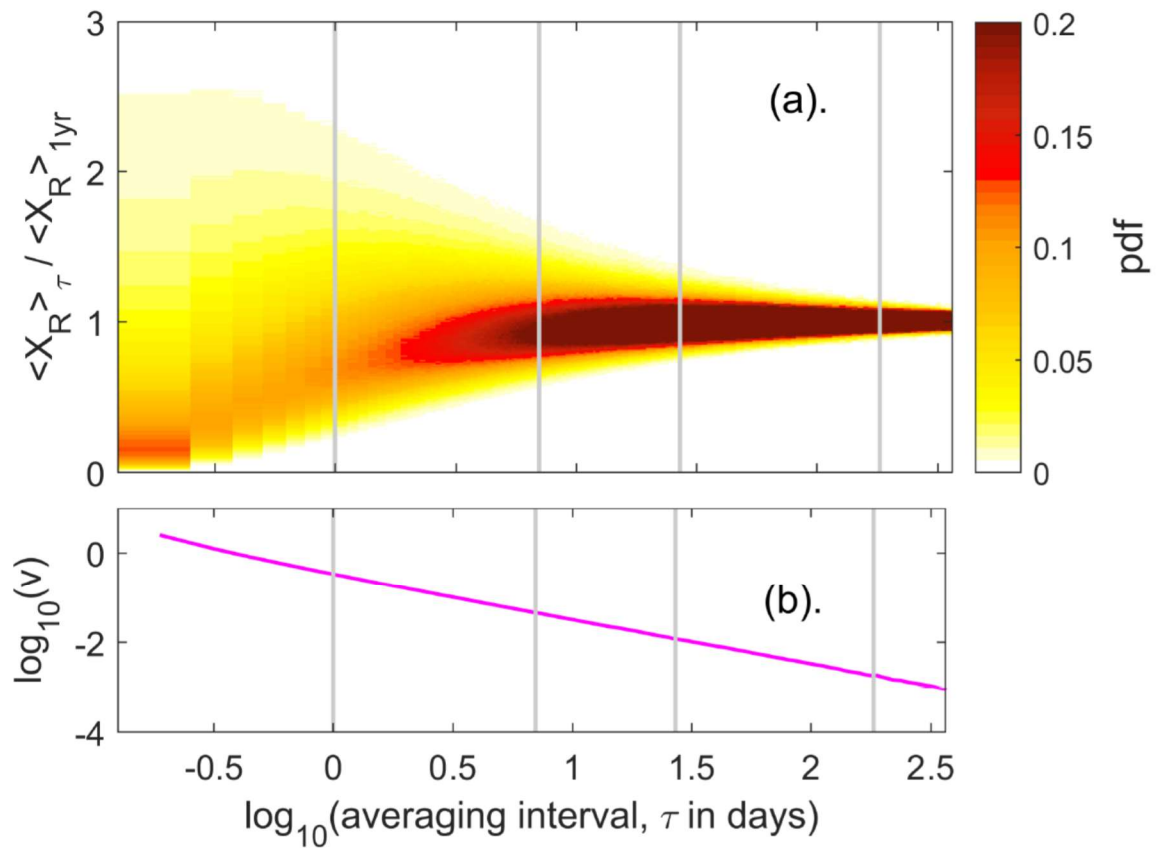
1084
 1085 **Figure 4.** The variation of the observed distributions of the normalized power input into the
 1086 magnetosphere $\langle P_{\alpha} \rangle_{\tau} / \langle P_{\alpha} \rangle_{1\text{yr}}$ for $\alpha = 0.44$) as a function of the logarithm of the averaging interval,
 1087 $\log_{10}(\tau)$. The left hand edge of the plot is at $\tau = 3$ hrs, the right hand edge at $\tau = 1$ yr., and the
 1088 vertical black lines show τ of 6 hours, 1 day, 7 days, 27 days and 0.5 year. (b) The logarithm of the
 1089 best-fit variance of the lognormal distribution (of mean value $m = 1$), $\log_{10}(v)$, also as a function of
 1090 $\log_{10}(\tau)$.



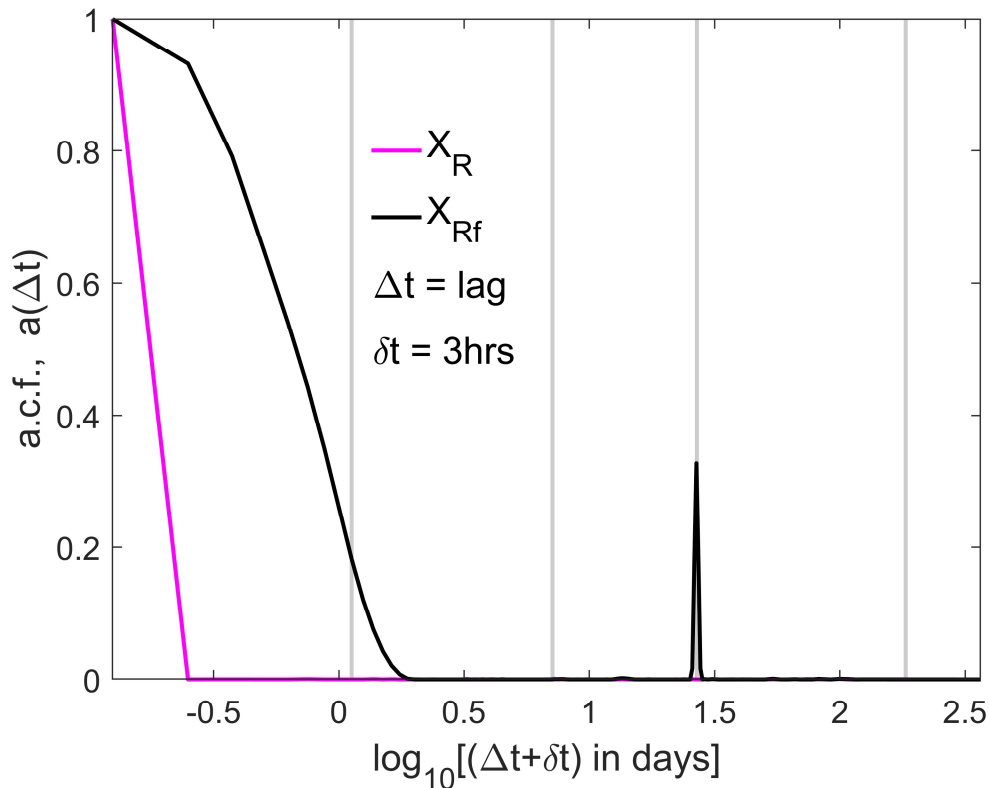
1091

1092 **Figure 5.** Same as Figure 4 for the normalized ap geomagnetic index, $\langle ap \rangle_{\tau} / \langle ap \rangle_{1\text{yr}}$. The
 1093 distributions for $\tau < 9$ hr. are not shown as the quantization of 3-hourly ap levels becomes a factor.

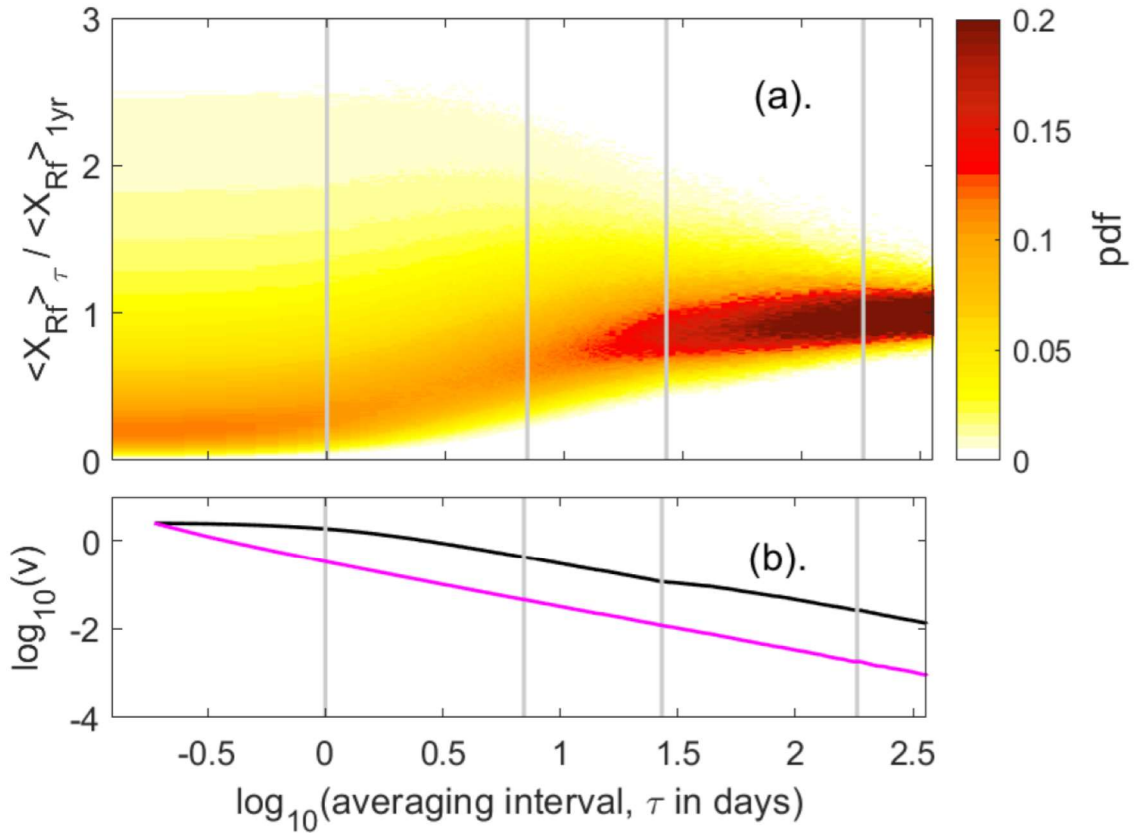
1094



1095
 1096 **Figure 6.** The same as Figure 4 for a random variable X_R of the same length and time resolution as
 1097 the P_α data series and which for $\tau = 3$ hr. is drawn from a Weibull distribution with k of 1.0625 and
 1098 λ of 1.0240, which in Paper 2 [Lockwood *et al.*, 2018c] was shown to be good fit to the distribution
 1099 of P_α at that timescale.
 1100

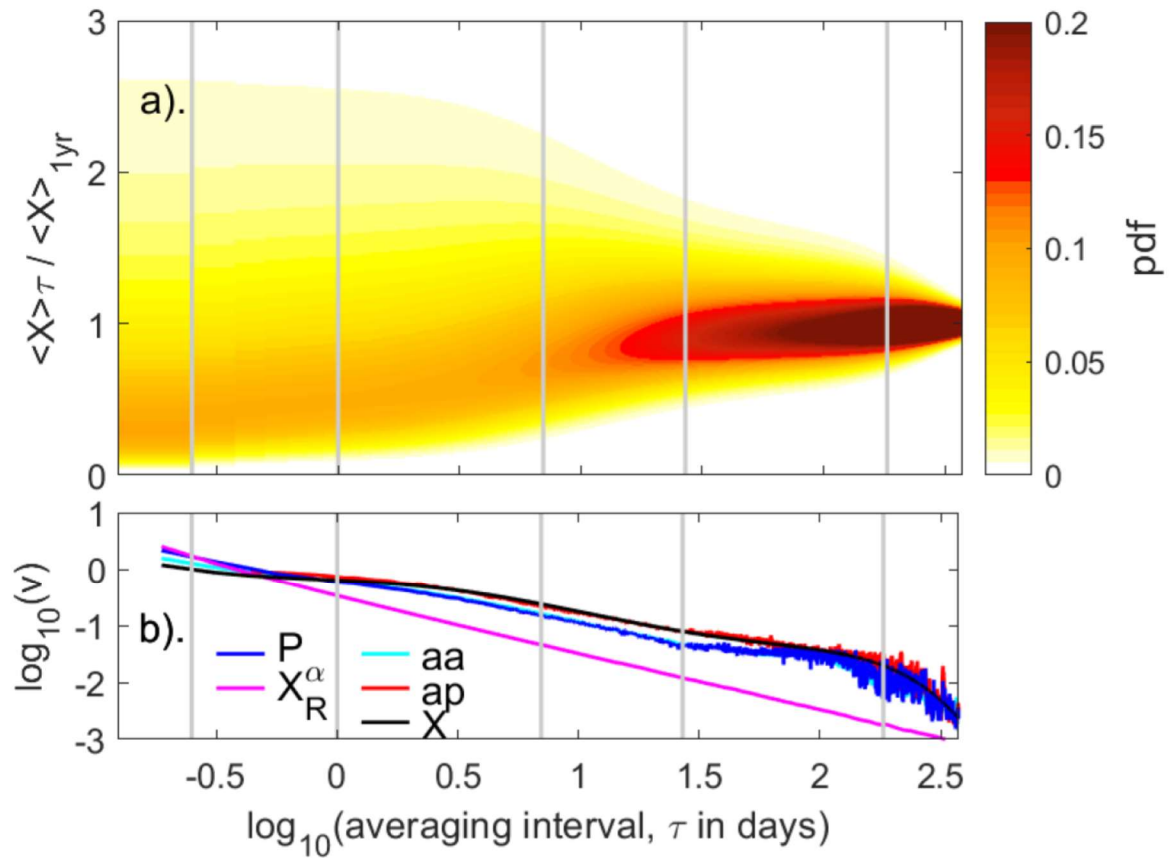


1101
 1102 **Figure 7.** The autocorrelation functions (ACFs) of (in mauve) the random variable X_R employed in
 1103 Figure 6 and (in black) the filtered random variable X_{Rf} employed in Figure 8. The ACF, $a(\Delta t)$ is
 1104 computed for lags Δt between zero and 1 year in steps of the data resolution ($\delta t=3$ hrs) and are
 1105 shown as a function of $\log_{10}(\Delta t+\delta t)$ where Δt and δt are both in units of days. (The δt is added to Δt
 1106 to allow the zero lag point to be shown on a logarithmic scale). The left hand edge of the plot is at
 1107 $\Delta t=0$ and the right hand edge at $\Delta t=1$ year and the vertical grey lines are at lags Δt of 1 day, 7
 1108 days, 27 days and 0.5 year. Lag 1 ($\Delta t=\delta t$) is at -0.602 on the x axis.



1109

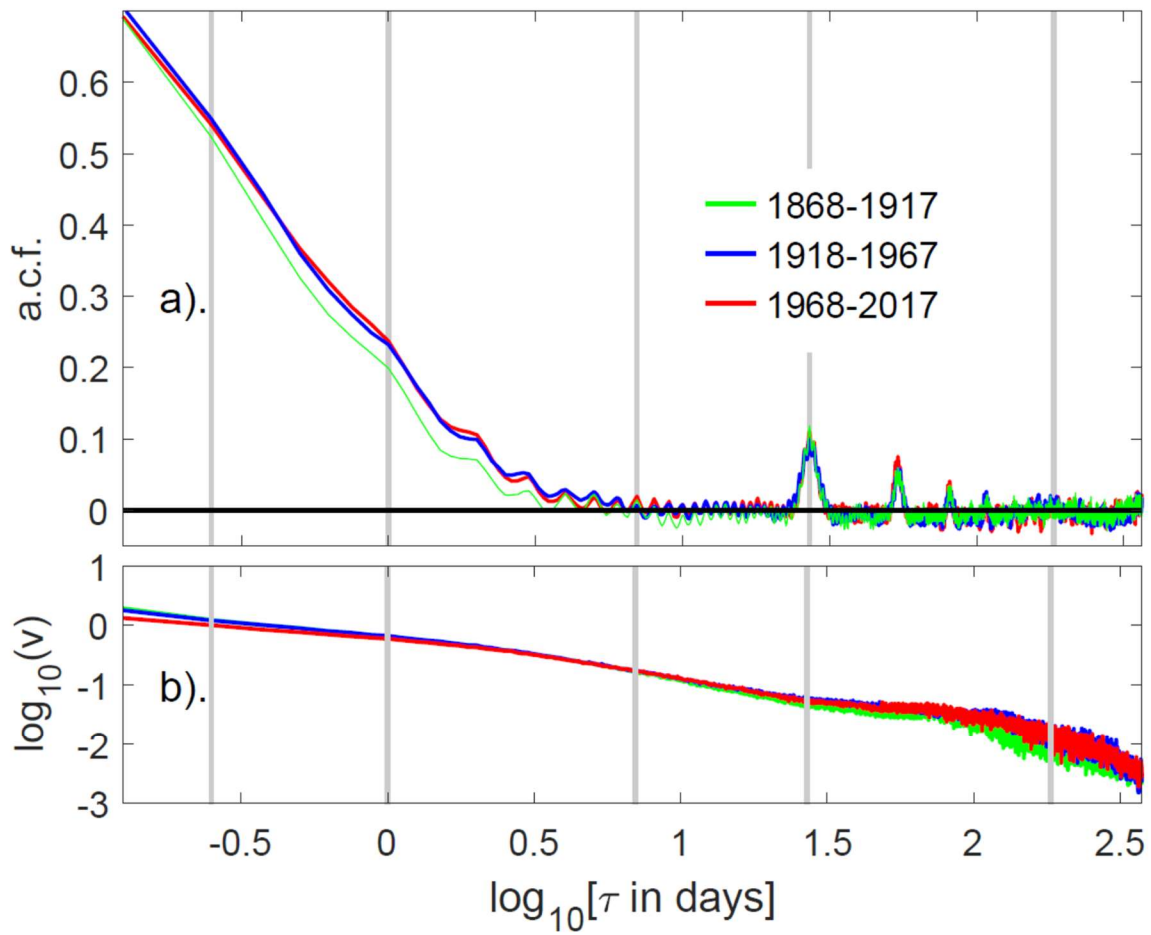
1110 **Figure 8.** The same as Figure 6 for a random variable X_{Rf} which has been drawn from a Weibull
 1111 distribution and then passed through a filter to generate the short-term persistence and the 27-day
 1112 recurrence shown by the autocorrelation function in blue in Figure 7 (see text for details of the
 1113 filter). In order that the distributions of X_{Rf} and X_R have the same variance at $\tau = 3$ hrs (with unity
 1114 mean), the effect of the filter means that before filtering the distribution must be drawn from a
 1115 higher-variance Weibull distribution (with unity mean) than X_R with k of 0.2800 and λ of 0.0778.
 1116 The black line in (b) shows the evolution of the variance, v , (on a logarithmic scale) with τ for X_{Rf}
 1117 and the blue line is the same variation for X_R , as shown in Figure 6(b).



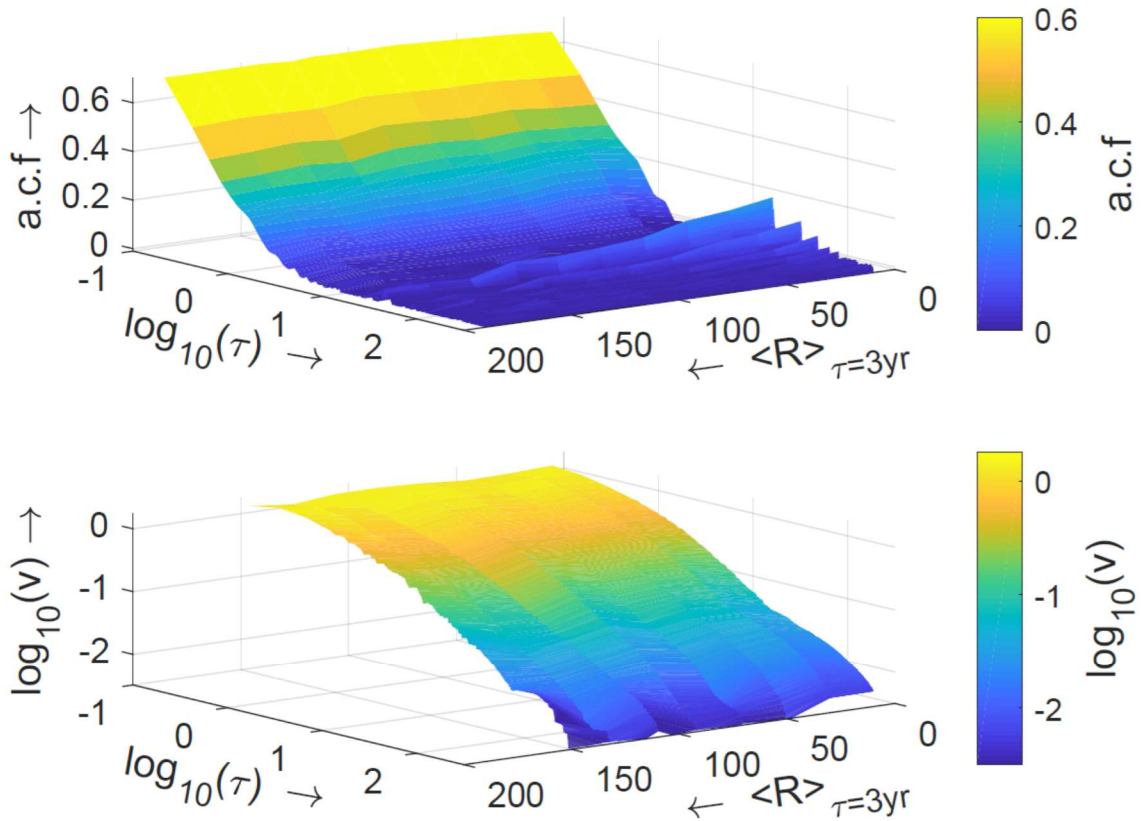
1118

1119 **Figure 9.** Same as Figure 5 for a model X based on lognormal distributions and a 6th-order
 1120 polynomial fit to the variance of ap , $\nu(\tau)$. In (b) the red line shows $\nu(\tau)$ for ap (on a logarithmic
 1121 scale) and the black line is the polynomial fit (see Appendix A for the polynomial coefficients and
 1122 formulae for the lognormal distribution family). Also shown are the $\nu(\tau)$ variations for other
 1123 variables using the same color scheme as used in Figures 4b, 5b and 6b: P_α (in blue); random
 1124 variable, X_R (in mauve), plus the aa geomagnetic index (in cyan).

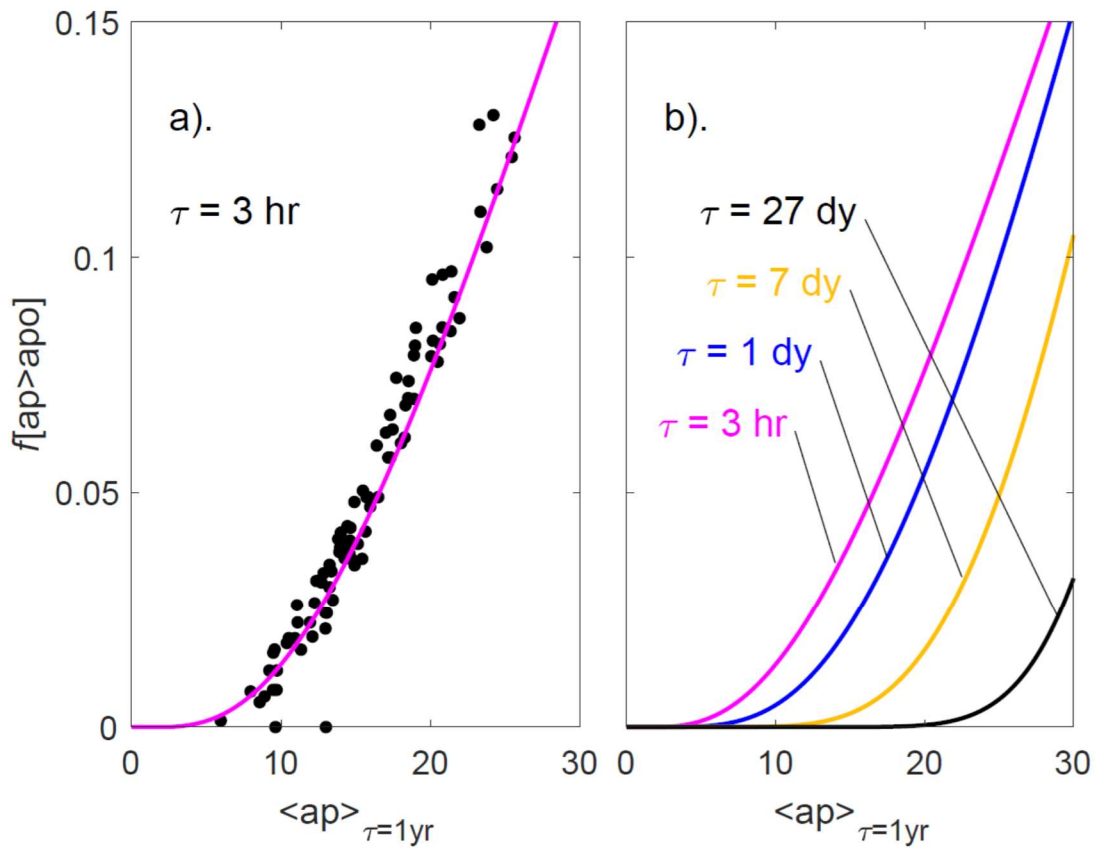
1125



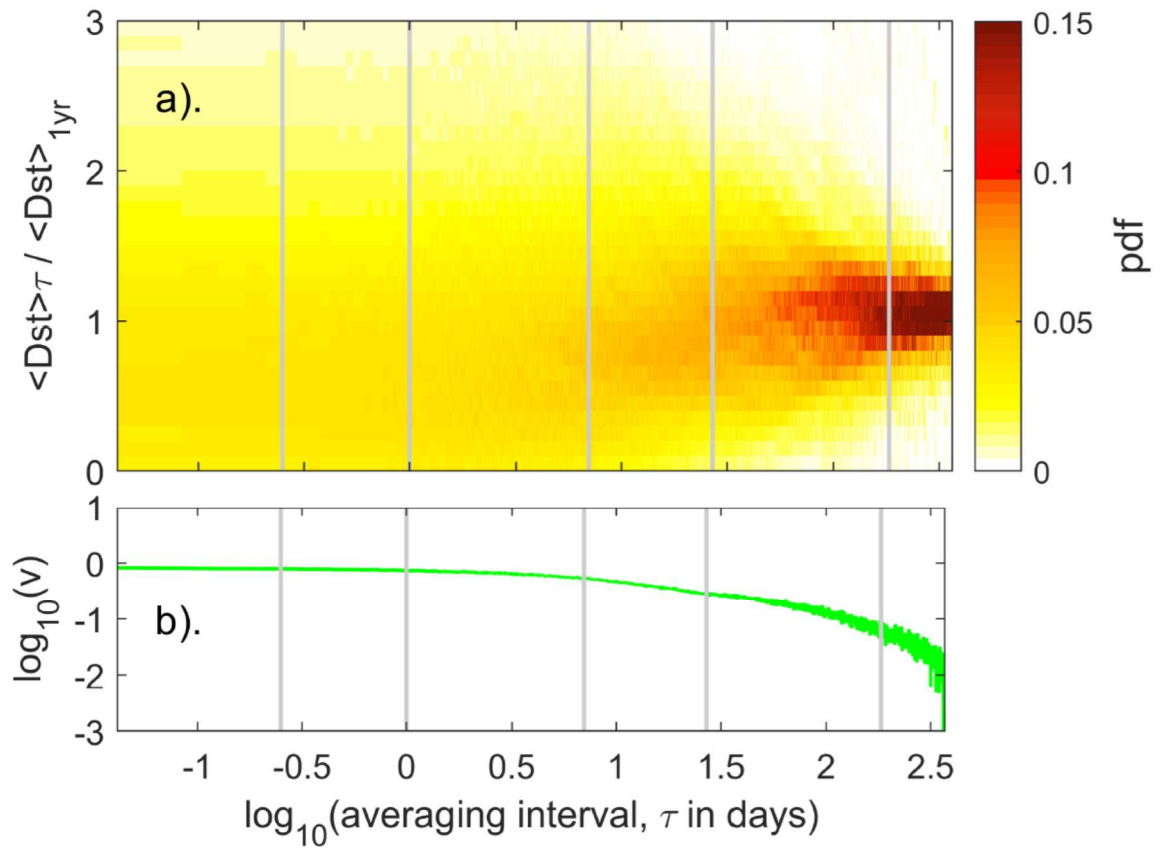
1126
 1127 **Figure 10.** (Top) The autocorrelation function of the 3-hourly *aa* index, divided into three 50-year
 1128 intervals: (red) 1968-2017 (inclusive); (blue) 1918-1967; and (green) 1868-1917. The lower panel
 1129 shows the relationship of the variance v of the lognormal distribution of $\langle aa \rangle_{\tau} / \langle aa \rangle_{\tau=1\text{yr}}$ as a
 1130 function of the averaging timescale (on the log-log plot format used in part (b) of Figures 4-9).



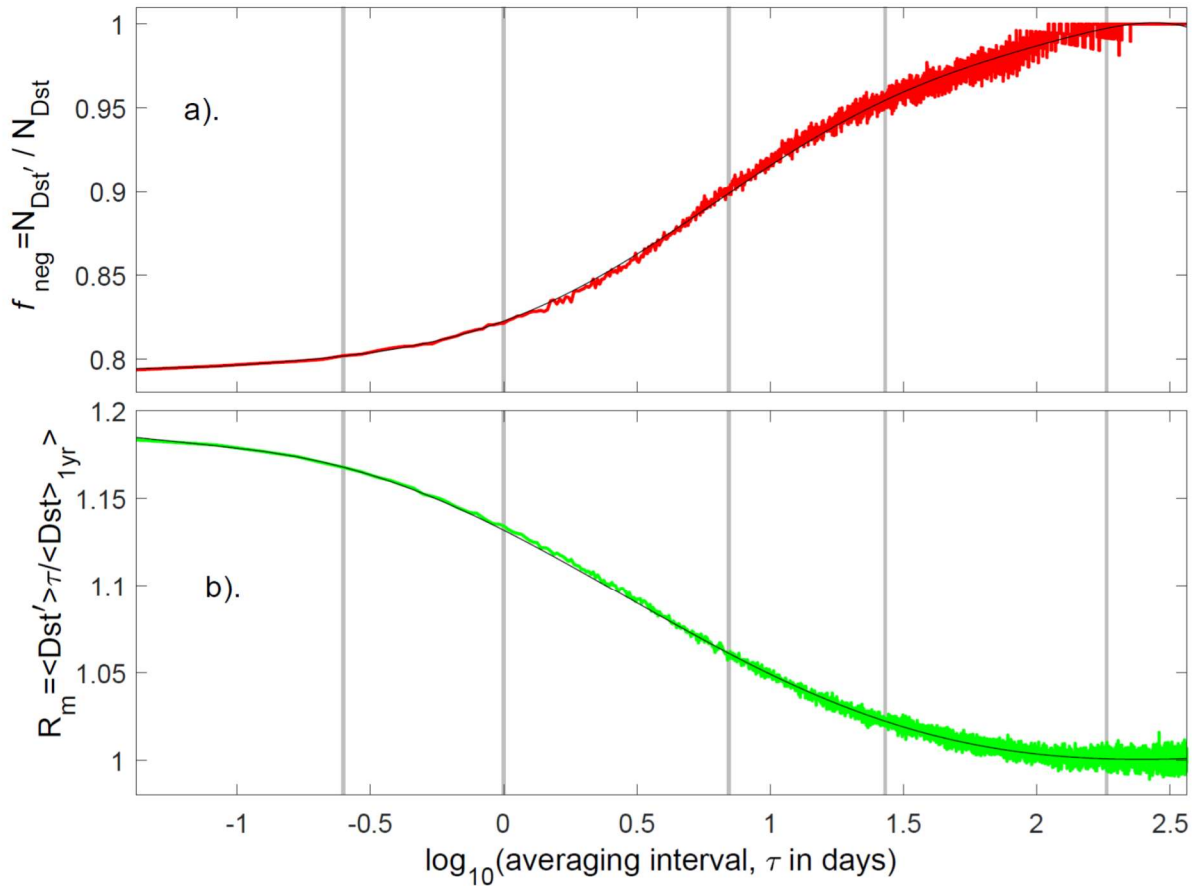
1131
 1132 **Figure 11.** Surface plots of (top) The autocorrelation function, ACF, and (bottom) the logarithm of
 1133 the variance, $\log_{10}(v)$, for all the *aa* index data (1868-2017) as a function of the logarithm of the
 1134 averaging timescale, $\log_{10}(\tau)$., and the mean international sunspot number, averaged over a 3-year
 1135 interval, $\langle R \rangle_{\tau=3\text{yrs}}$.



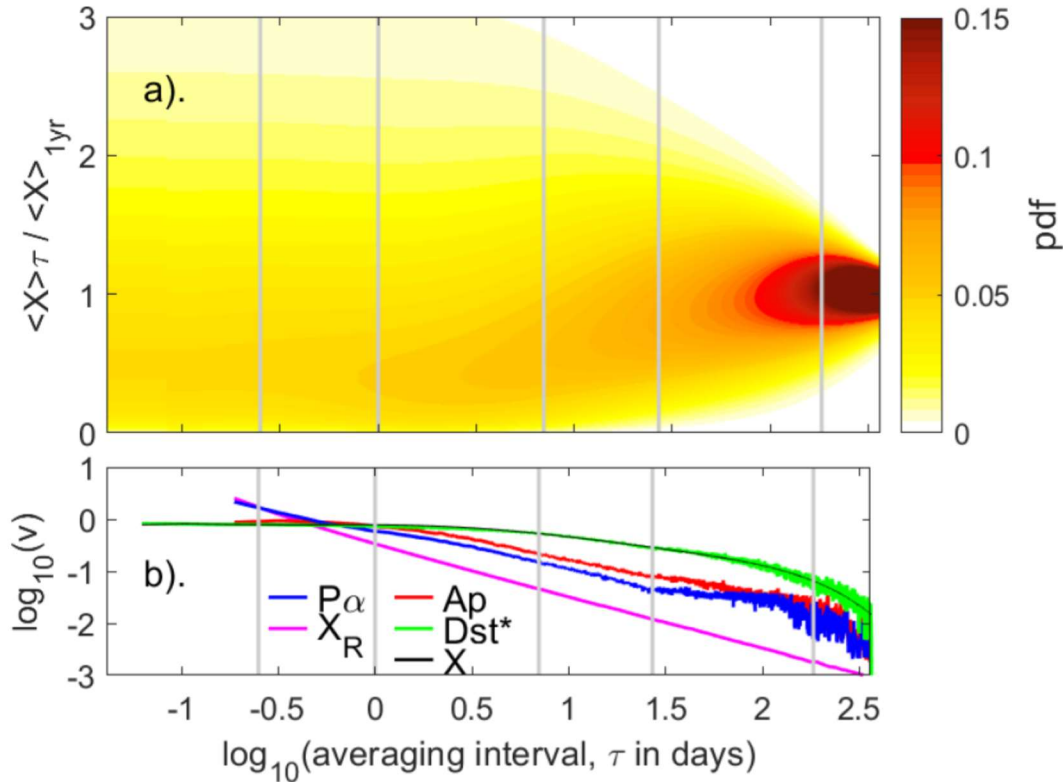
1136
 1137 **Figure 12.** Predictions by the model fit to the ap distributions with τ shown in Figure 9. (a) The
 1138 points show probability that 3-hour values of ap are in the top 5% of the overall distribution (for
 1139 1932-2016, 252152 samples), $f[ap > apo]$ (i.e., ap exceeds its 95-percentile of 3-hourly ap values,
 1140 $apo = 47.91$), as a function of the annual mean value $\langle ap \rangle_{\tau=1yr}$. The mauve line is the model
 1141 prediction for $\tau=3$ hrs. (b). The family of model predictions of $f[ap > apo]$ as a function of $\langle ap \rangle_{\tau=1yr}$
 1142 for timescales τ of 3 hours (in mauve), 1 day (in blue), 7 days (in orange) and 27 days (in black).



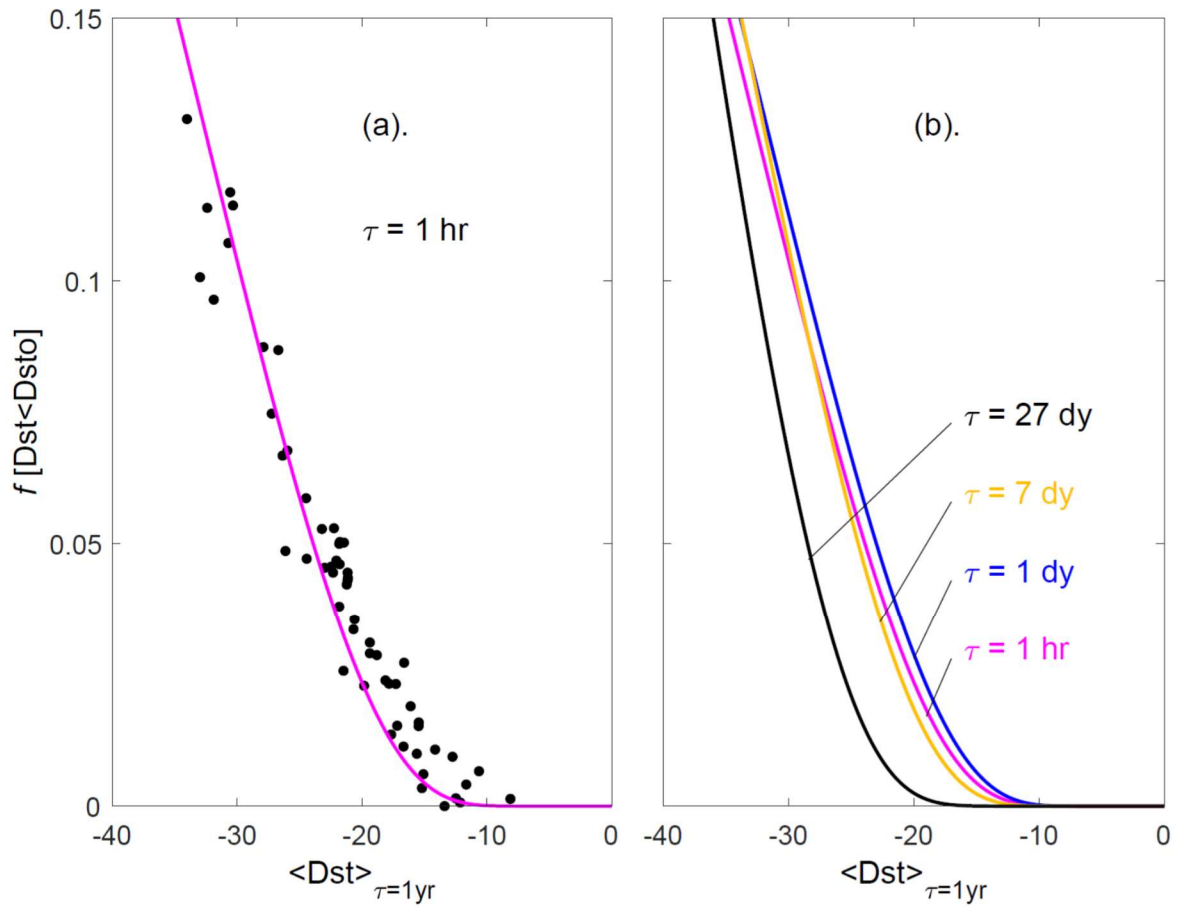
1143
 1144 **Figure 13.** Same as Figure 4 for the normalized Dst geomagnetic index, $\langle Dst' \rangle_{\tau} / \langle Dst \rangle_{1yr}$ where
 1145 Dst' is the subset of Dst values that are negative.



1146
 1147 **Figure 14.** The variation with averaging interval τ of (top) the fraction of Dst samples that are
 1148 negative (the subset termed Dst') and (bottom) the mean of the ratio of the mean value of Dst' in
 1149 intervals of duration τ , to the annual mean values of Dst . (a) $f_{\text{neg}} = N_{Dst'} / N_{Dst}$ is shown as a function
 1150 of $\log_{10}(\tau)$, where $N_{Dst'}$ is the number of samples at that τ for which $Dst \leq 0$ and N_{Dst} is the number
 1151 of Dst samples of either sign. The red line is the mean for all Dst samples (from 1957-2016), the
 1152 black line is best polynomial fit (see Appendix A for details). (b) $R_m = \langle Dst' \rangle_{\tau} / \langle Dst \rangle_{1\text{yr}}$ is shown
 1153 as a function of $\log_{10}(\tau)$. The green line shows the result for all the data (from 1957-2016), the
 1154 black line is best polynomial fit (see Appendix A for details).



1155
 1156 **Figure 15.** Same as Figure 9 for a model X based on Weibull distributions and a 6th-order
 1157 polynomial fit to the variance of Dst' , $\nu(\tau)$. Note that by only considering the negative Dst values
 1158 (Dst') the mean values of the fitted distributions are $R_m(\tau)$ rather than unity and pdfs have also
 1159 been multiplied by f_{neg} to allow for existence of positive values – in both cases, the values used here
 1160 from the polynomial fits shown in Figure 14. In (b) the green line shows $\nu(\tau)$ for Dst' (on a
 1161 logarithmic scale) and the black line is the polynomial fit (see Appendix A for the polynomial
 1162 coefficients and *formulae* for the Weibull distribution family). Also shown are the $\nu(\tau)$ variations
 1163 for other variables using the same color scheme as used in Figures 4b, 5b and 6b: P_α (in blue); ap
 1164 (in red); random variable, X_R (in mauve).



1165
 1166 **Figure 16.** Same as Figure 12 for predictions by the model fit to the Dst distributions with τ shown
 1167 in Figure 15. (a) The points show the observed probability that 1-hour values of Dst are in the top
 1168 5% of the overall distribution of Dst disturbance levels (for 1957-2016, 525960 samples),
 1169 $f [Dst < Dsto]$ (i.e. Dst is less than its 5-percentile of 1-hourly values, $Dsto = -55.14$ nT), as a
 1170 function of the annual mean value of Dst values $\langle Dst \rangle_{\tau=1yr}$. The mauve line is the model prediction
 1171 for $\tau = 1$ hrs. (b). The family of model predictions of $f [Dst < Dsto]$ as a function of $\langle Dst \rangle_{\tau=1yr}$ for
 1172 timescales τ of 1 hour (in mauve), 1day (in blue), 7 days (in orange) and 27 days (in black).
 1173

1174 **Appendix A. Probability distributions of ap and Dst**

1175 In the paper, we make use of two distribution forms, the Lognormal and the Weibull

1176 **(A-i). The equations of the Lognormal Distribution**

1177 For the lognormal distribution the two parameters that are usually used to specify the distribution
1178 are μ and σ . These are, respectively, the mean and standard deviation of the normal distribution in
1179 $\log_n(x)$ where x is the variable that is lognormally distributed. These are related to the mean m and
1180 variance v of x by

$$1181 \quad m = \exp(\mu + \sigma^2/2) \quad (A1)$$

$$1182 \quad v = [\exp(\sigma^2 - 1)] \times \exp(2\mu + \sigma^2) \quad (A2)$$

1183 or conversely expressing μ and σ in terms of m and v we have

$$1184 \quad \mu = \log_n (m / (1 + v/m^2)^{1/2}) \quad (A3)$$

$$1185 \quad \sigma^2 = \log_n (1 + v/m^2) \quad (A4)$$

1186 Hence specifying a lognormal distribution using μ and σ is precisely the same as specifying it using
1187 m and v . The advantage of using μ and σ is that the equation for the probability distribution of a
1188 lognormal is simpler:

$$1189 \quad f(x) = \{1/x\} \times \{1/(2\pi\sigma^2)^{1/2}\} \times \exp\{(-\log_n(x) - \mu)^2 / (2\sigma^2)\} \quad (A5)$$

1190 For any one combination of m and v , we compute μ and σ using equations (A3) and (A4) and hence
1191 determine the full distribution using (A5).

1192 **(A-ii) The equations for a Weibull Distribution**

1193 For Weibull distribution (also called the Rosin Rammler distribution), the two parameters used to
1194 describe the distribution are a scale parameter λ and a shape parameter k . (Note that both λ and k
1195 are always positive).

1196 The mean and variance of the distribution in x are again m and v , where

$$1197 \quad m = \lambda \Gamma(1 + 1/k) \quad (A6)$$

$$1198 \quad v = \lambda^2 \{ \Gamma(1 + 2/k) - (\Gamma(1 + 1/k))^2 \} \quad (A7)$$

1199 Where Γ is a gamma function. The converse equations for λ and k cannot be derived analytically
 1200 and we solve them iteratively by varying the shape parameter k until

$$1201 \quad \lambda = m / \{\Gamma(1+1/k)\} \quad (A8)$$

1202 and

$$1203 \quad \Gamma(1+2/k) = (v + m^2) / \lambda^2 \quad (A9)$$

1204 and then checking the full range of allowed k for a given v and m that the solution is unique.

1205 The Weibull distribution is:

$$1206 \quad f(x) = (k/\lambda) \times (x/\lambda)^{k-1} \times \exp\{-(x/\lambda)^k\} \quad \text{for } x \geq 0$$

$$1207 \quad f(x) = 0 \quad \text{for } x < 0 \quad (A10)$$

1208 Hence, as for the lognormal, the distribution is described by two parameters (μ and σ for a lognormal
 1209 and k and λ for a Weibull) and in both cases specifying that pair is fully equivalent to specifying the
 1210 mean and the variance. Note that in the paper we fit variables of the form $X/\langle X \rangle$ and so the mean
 1211 value is $m = 1$ and the one fit variable is the variance v . The remainder of this Appendix gives the
 1212 models used to generate the probability distribution functions, as a function of averaging timescale,
 1213 τ , for the ap and Dst geomagnetic indices, shown in Figures 9 and 15, respectively.

1214 (A-iii) Model for ap

1215

1216 The polynomial fit to the variation of the logarithm of the variance, v , with timescale τ for the ap
 1217 index, shown by the black line in Figure 9b, gives

$$1218 \quad \log_{10}(v) = \beta = -0.0471\tau^6 + 0.1309\tau^5 + 0.0954\tau^4 - 0.3554\tau^3 - 0.1651\tau^2 - 0.2124\tau + 0.2048 \quad (A11)$$

1219 such that the model variance is

$$1220 \quad v(\tau) = 10^\beta \quad (A12)$$

1221 By normalizing the ap values by the annual mean $\langle ap \rangle_\tau / \langle ap \rangle_{\tau=1\text{yr}}$, the annual distributions have a
 1222 mean $m = 1$ at all τ

1223 For ap the best fit is with the family of lognormal distributions.

$$1224 \quad \eta = 1 + (v/m^2) \quad (A13)$$

$$1225 \quad \mu = \log(m/\eta^{0.5}) \quad (A14)$$

$$1226 \quad \sigma = \log_n^{0.5}(\eta) \quad (A15)$$

$$1227 \quad x = \langle ap \rangle_\tau / \langle ap \rangle_{\tau=1\text{yr}} \quad (A16)$$

$$1228 \quad a = (x\sigma(2\pi)^{0.5})^{-1} \quad (A17)$$

$$1229 \quad b = \exp\{(-(\log(x)-\mu^2)/(2\sigma^2))\} \quad (A18)$$

$$1230 \quad f(x,\tau) = ab, \quad f(0,\tau) = 0 \quad (A19)$$

1231 The equations (A11) - (A19) allows the computation of the pdf f for a value of ap for an averaging
1232 timescale τ , $\langle ap \rangle_\tau$, if we know its annual mean, $\langle ap \rangle_{\tau=1\text{yr}}$.

1233 Comparison of Figures 5a and 9a of the main text demonstrate the fit of the family of distributions
1234 to the ap data.

1235 **(A-iv) Model for Dst**

1236
1237 The polynomial fit to the variation of the logarithm of the variance, ν , with timescale τ for the Dst
1238 index, shown by the black line in Figure 15b, gives:

$$1239 \quad \beta = -0.0158\tau^6 + 0.0353\tau^5 + 0.0462\tau^4 - 0.1283\tau^3 - 0.1387\tau^2 - 0.0318\tau - 0.1060 \quad (A20)$$

1240 such that the model variance is

$$1241 \quad \nu(\tau) = 10^\beta \quad (A21)$$

1242 The fraction of Dst' samples (with $Dst \leq 0$), as a function of timescale τ is given by the polynomial
1243 (the black line in Figure 14a)

$$1244 \quad f_{\text{neg}} = -0.0003\tau^8 + 0.0004\tau^7 + 0.0035\tau^6 - 0.0039\tau^5 - 0.0161\tau^4 + 0.0052\tau^3 + 0.0461\tau^2 + 0.0578\tau + 0.8226$$

$$1245 \quad (A22)$$

1246 (Note that such a high-order polynomial is needed to capture the observed variation with sufficient
1247 accuracy).

1248 The polynomial fit to the ratio of the means of Dst' for intervals of length τ , $\langle Dst' \rangle_\tau$ (where
1249 Dst' is the subset of Dst values that are negative), and the annual mean of Dst , $\langle Dst \rangle_{1\text{yr}}$ given by
1250 the black line in Figure 14b, is

$$1251 \quad R_m = \langle Dst' \rangle_\tau / \langle Dst \rangle_{1\text{yr}} = 0.0003\tau^6 - 0.0024\tau^5 + 0.0033\tau^4 + 0.0145\tau^3 - 0.0215\tau^2 - 0.0770\tau - 1.1319$$

$$1252 \quad (A23)$$

1253 For Dst' , the best fit is with the family of Weibull distributions, the variance of which is

$$1254 \quad v(k) = \lambda^2 \{ \Gamma(1+2/k) - (\Gamma(1+1/k))^2 \} \quad (A24)$$

1255 where Γ is a gamma function. The best method is to find the factor k is by iteration to the value that
1256 gives

$$1257 \quad v_m(\tau) = v(k) \quad (A25)$$

1258 Note that the mean of the distribution is, unlike for the *ap* case, not in general unity because of the
1259 exclusion of the positive *Dst* values. Rather, the mean is R_m given by equation (A23). This yields

$$1260 \quad \lambda = R_m / \Gamma(1+1/k) \quad (A26)$$

$$1261 \quad x = \langle Dst' \rangle_{\tau} / \langle Dst \rangle_{\tau=1yr} \quad (A27)$$

$$1262 \quad a = k/\lambda \quad (A28)$$

$$1263 \quad b = (x/\lambda)^{k-1} \quad (A29)$$

$$1264 \quad c = \exp(-(x/\lambda)^k) \quad (A30)$$

$$1265 \quad f_w(x, \tau) = f_{neg} \cdot a \cdot b \cdot c \quad (\text{always valid as } x \geq 0) \quad (A31)$$

1266 The normalising factor f_{neg} (given by equation (A22) for a given τ) is needed because the product of
1267 the terms a , b and c gives the pdf of Dst' , but they are only a fraction f_{neg} of the whole *Dst* sample.

1268 The equations (A10) - (A21) allows the computation of the p.d.f. f for a negative value of *Dst* for an
1269 averaging timescale τ , $\langle Dst' \rangle_{\tau}$, for an annual mean of *Dst*, $\langle Dst \rangle_{\tau=1yr}$.

1270 Comparison of Figures 13a and 15a demonstrate the fit of the family of distributions to the *Dst*
1271 data.

1272 **Appendix B. Relationship of daily means of aa and ap and correcting ap**

1273 Figure B-1 shows scatter plots of daily means of the ap index (by convention referred to as Ap) in
 1274 3-month intervals a function of the simultaneous daily mean of the aa index. This plot is restricted
 1275 to data from between 1932 (the start of the ap index data) and 1956 (inclusive). The end date is
 1276 because in 1957 there is a calibration error in aa introduced by the move of the northern hemisphere
 1277 aa station from Abinger to Hartland. This has been corrected using the ap index by *Lockwood et al.*
 1278 [2014] and *Matthes et al.* [2017] – hence it is not appropriate to use data for 1957 and after, either
 1279 with or without that correction. There is considerable scatter about the trend in figure B-1, much of
 1280 which is introduced by different annual responses of the two indices associated with the different
 1281 geographic distribution of stations. Note there are also considerable diurnal differences also, but
 1282 there are averaged out by taking daily means (which are Ap for ap and Aa for aa). The relationship
 1283 between Aa and Ap depends on time-of-year (see Figure B-1) and the best-fit polynomials to the
 1284 data for 4 fraction of year intervals, each covering a quarter of a year and centred on the times of
 1285 the March equinox, June solstice, September equinox and December solstice are:

1286 $0.09 \leq F \leq 0.34 \quad Ap^* = (7.241 \times 10^{-7})Aa^{*3} - (1.351 \times 10^{-3})Aa^{*2} + 1.108Aa^* - 8.410 \quad (B1)$

1287 $0.34 \leq F \leq 0.59 \quad Ap^* = (8.959 \times 10^{-7})Aa^{*3} - (1.597 \times 10^{-3})Aa^{*2} + 1.182Aa^* - 9.236 \quad (B2)$

1288 $0.60 \leq F \leq 0.85 \quad Ap^* = (7.131 \times 10^{-7})Aa^{*3} - (1.344 \times 10^{-3})Aa^{*2} + 1.127Aa^* - 8.539 \quad (B3)$

1289 $F \leq 0.12$ or $F \geq 0.8 \quad Ap^* = (6.621 \times 10^{-7})Aa^{*3} - (1.156 \times 10^{-3})Aa^{*2} + 0.907Aa^* - 4.969 \quad (B4)$

1290 These polynomial fits and plus and minus their 2-sigma errors are shown in Figure B-1 (as solid
 1291 and dashed lines, respectively). For the estimated Aa^* of the Carrington event [*Cliver and*
 1292 *Svalgaard, 2004*], these fits yield Ap^* of 275 ± 24 , 277 ± 44 , 283 ± 30 and 224 ± 33 for the March
 1293 equinox, June solstice, September equinox and December solstice data, respectively.

1294 Our research into the response functions of geomagnetic indices (the collective response of the
 1295 network of stations used to generate them and of the compilation algorithm used to combine the
 1296 data from them) using the model of *Lockwood et al.* [2018d, e] has shown that the am geomagnetic
 1297 index has a very flat, almost ideal, time-of-day/ time-of-year response. This is achieved because
 1298 this index employs relatively uniform rings of mid-latitude stations in both hemispheres and uses

1299 weighted means to account for any spatial non-uniformity of the station network. On the other
 1300 hand, the compilation of the *ap* index employs an irregular network of predominantly northern
 1301 hemisphere (mainly European) stations and look-up tables to convert the observations from each
 1302 into the value that would be seen at the reference Niemegek station before combining them by
 1303 averaging. The look-up tables are specific to the station location and depend on time-of-day (UT),
 1304 time-of-year (*F*) and the level of the activity. *Cliver and Svalgaard* [2004] recognized the value of
 1305 the *am* index, compared to indices derived from less-ideal distributions of stations, and used it to
 1306 correct for the false time-of-day variation in the *aa* index (and so created what they termed *aa_m*).
 1307 However, they did not correct for the associated spurious time-of-year variation in *aa* [*Lockwood et*
 1308 *al.*, 2018e] and then used the suggestion of *Allen* [1982] of 24-hour running means of *aa_m* (which
 1309 they termed *Aa_m**) which largely suppresses the false UT variation anyway. We here apply the
 1310 same philosophy that *Cliver and Svalgaard* [2004] adopted, but use *am* to correct for any false
 1311 time-of-year variation in *ap*. We do this because the *am* index data only extends back to 1959
 1312 whereas the *ap* index is available from 1932 onward.

1313 We have generated a corrected *ap* index, *ap_C*, which allows for effects as a function of the fraction
 1314 of each year (*F*) and the *ap* level using the formula

$$1315 \quad ap_C(F) = ap(F) \times \underline{C}_{ap}(F,ap) \quad (B5)$$

1316 where the correction factor is given by

$$1317 \quad C_{ap}(F,ap) = (\langle am(F,ap) \rangle_{bin} / \langle am \rangle_{all}) / (\langle ap(F,ap) \rangle_{bin} / \langle ap \rangle_{all})$$

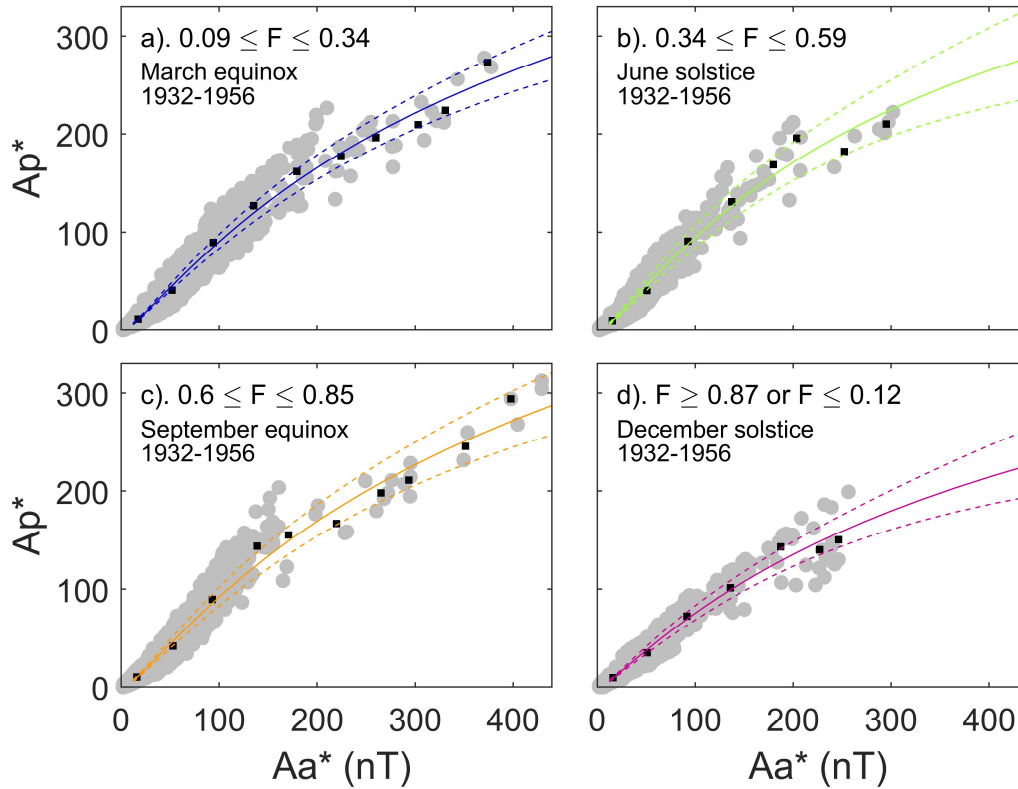
$$1318 \quad = (\langle am(F,ap) \rangle_{bin} / \langle ap(F,ap) \rangle_{bin}) \times (\langle ap \rangle_{all} / \langle am \rangle_{all}) \quad (B6)$$

1319 The subscript “all” refers to the averaging of all co-incident *ap* and *am* data for 1959-2017
 1320 (inclusive) and the subscript “bin” refers to the averaging of data in a given *F* and *ap* bin during the
 1321 same interval. Multiplying by the ratio of the all-over means of *ap* and *am* means that we correct for
 1322 the variation with *F* but do not change the average levels of *ap*. In practice, the data were divided
 1323 into 40 percentiles of the overall *ap* distribution, giving 6282 samples in each *ap* bin, the values of
 1324 $C_{ap}(F,ap)$ were then fitted with a 6th order polynomial in *F*. The derived correction factor $C_{ap}(F,ap)$
 1325 is shown as a function of *F* (*x* axis) and $\log_{10}(Ap)$ (*y* axis) in figure B-2. Note that we are not

1326 concerned with any limitations in the UT dependence of the response of ap because we use
1327 averages over 24-hour intervals, as discussed below. This correction is only approximate because
1328 the network of stations used to generate the ap index has changed several times since 1932.
1329 However, we do not find any detectable discontinuities in $C_{ap}(F,ap)$ at any of the changes since
1330 1959 and so we use the assumption that effects of changes before this date also have negligible
1331 effect. The effect of the correction is not great (see Figure B-3) but is largest for the most active
1332 days. Many of these storm day values are hardly altered by the correction but those in northern
1333 hemisphere winter, in particular, are underestimated in ap and this is corrected in ap_C .

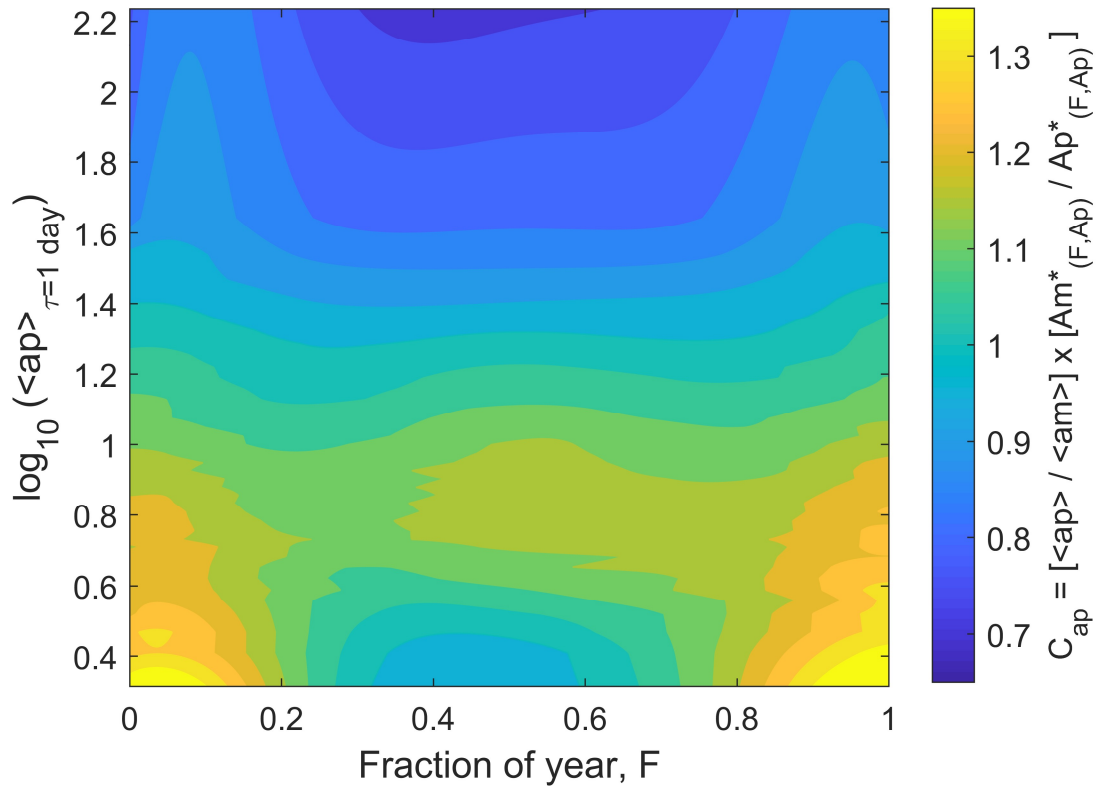
1334 We follow the procedure of *Allen* [1982] to make 24-hour boxcar means of ap_C , Ap_C^* . For the
1335 purposes of identifying and ranking storm days we take the largest value of the 8 such running-
1336 means in each calendar day $[Ap_C^*]_{MAX}$. The 100 largest values of $[Ap_C^*]_{MAX}$ since 1932 are given
1337 in rank order in Table S7 of the Supporting Information file. Although there are similarities, this
1338 list has a somewhat different ranking order to previous studies [e.g., *Nevanlinna et al.*, 2006;
1339 *Kappenman*, 2005; *Cliver and Svalgaard*, 2004], largely because of the allowance we make for the
1340 variation of the ap index response with time of year. Note that even quite small changes in the
1341 estimated magnitude of the storm day can have a very large effect on its position in the ranking
1342 order.

1343

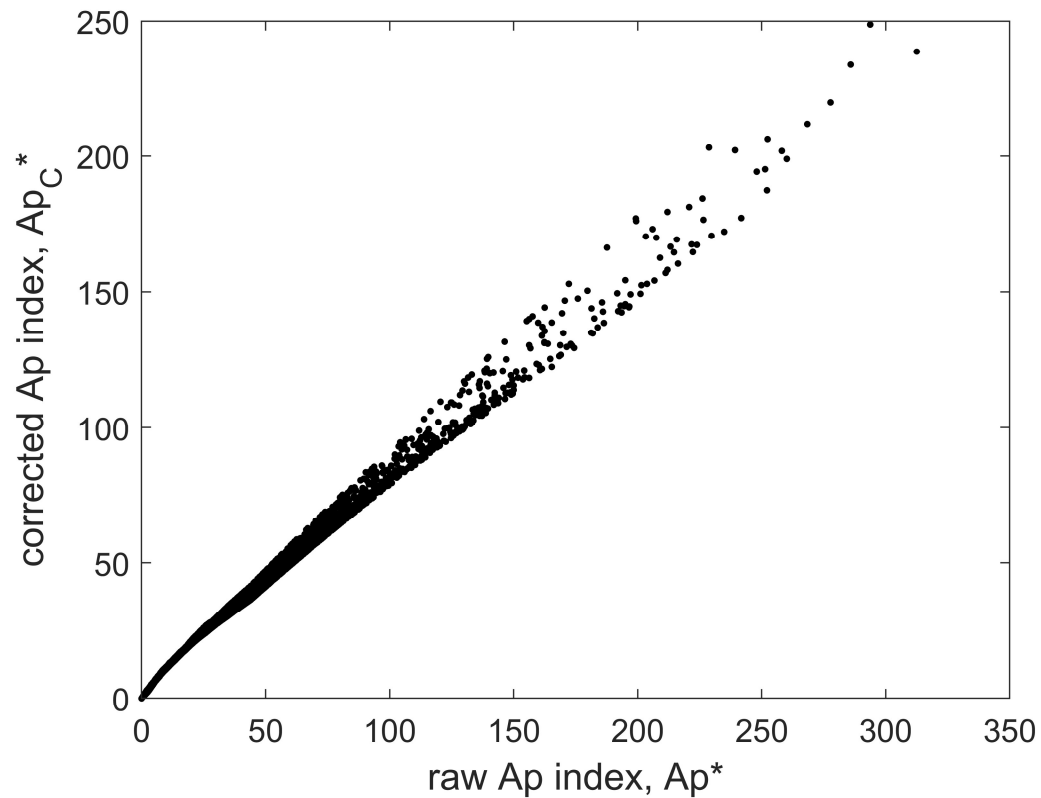


1344

1345 **Figure B-1.** Scatter plots of 24-hour means of the ap geomagnetic index, Ap^* , as a function of the
 1346 corresponding means of the aa index, Aa^* , for 1932-1956 (inclusive) for 0.25-yr intervals around
 1347 (a). March equinox; (b) June solstice; (c) September equinox and (d) December solstice. Black
 1348 squares are means over aa bins 40 nT wide. The solid lines are third order polynomial fits and the
 1349 dashed lines are plus and minus the best-fit 2-sigma error.



1350
 1351 **Figure B-2.** The Ap^* correction factor $C_{ap} = (Am^*/Ap^*) \cdot (\langle ap \rangle / \langle am \rangle)$ as a function of the time of
 1352 year, F , and the ap level (shown here on a logarithmic scale) derived from all the coincident ap and
 1353 am index data (for 1959-2017, inclusive).



1354
 1355 **Figure B-3.** The effect of correcting 24-hour means of the *ap* index for its dependence on time of
 1356 year, *F*: a scatter plot of Ap_C^* (8-point running means of the corrected $ap_C = ap \cdot C_{ap}$) as a function of
 1357 the corresponding running means of the original *ap* values, Ap^* . The plot is for all *ap* index data to
 1358 date (1932-2017, inclusive).